

GROUND PLANE SLOT STRUCTURES FOR ISOLATION OF COSITED
MICROSTRIP ANTENNAS

BY

KIERSTEN C. KERBY

B.S., University of Illinois at Urbana-Champaign, 2003

M.S., University of Illinois at Urbana-Champaign, 2005

DISSERTATION

Submitted in partial fulfillment of the requirements
for the degree of Doctor of Philosophy in Electrical and Computer Engineering
in the Graduate College of the
University of Illinois at Urbana-Champaign, 2009

Urbana, Illinois

Doctoral Committee:

Professor Jennifer T. Bernhard, Chair

Professor Andreas C. Cangellaris

Professor P. Scott Carney

Professor Steven J. Franke

ABSTRACT

Ground plane slot structures have been shown to reduce coupling between cosited antennas. Although some such structures have already been reported, no analytical model exists to describe their behavior and there are no design guidelines. In this work, the behavior of reported ground plane structures is used as a clue to obtain generalizable information about such structures' behavior. The structures' scalability and excitation behavior is investigated. Next a circuit model is derived that describes the interaction of microstrip patch antennas with a ground plane slot structure based on mutual admittances between the ground plane slots and the effective slots at the antennas' radiating edges. The circuit model leads to design guidelines for the ground plane slot structure and an approximate relationship between mutual admittances which must be satisfied in order to isolate the antennas. Finally, we present a novel ground plane slot structure that mitigates some of the disadvantages of earlier designs.

For Feanil and my parents

ACKNOWLEDGMENTS

I am grateful to my advisor, Professor Jennifer Bernhard, for her guidance in this and all my other academic endeavors. I also sincerely thank Tyrone Roach for his help with fabrication and measurement and Jessica Ruyle for her collaboration on the development of the circuit model. This work was supported by a Bell Labs Graduate Research Fellowship.

TABLE OF CONTENTS

LIST OF FIGURES	vii
CHAPTER 1 INTRODUCTION AND BACKGROUND	1
1.1 Introduction	1
1.2 Background: Reported Designs	2
CHAPTER 2 COMPARISON OF REPORTED GROUND PLANE SLOT STRUCTURES	6
2.1 Designs for Comparison	6
2.2 Base Configuration Design Discussion	8
2.3 Ground Plane Slot Design Scaling	11
2.4 Simulated Results and Comparison	14
2.4.1 Isolation	14
2.4.2 Undesired radiation	15
2.5 Conclusions	18
CHAPTER 3 INVESTIGATION OF GROUND PLANE SLOT STRUCTURE EXCITATION	19
3.1 Initial Frequency Response to Scaling	19
3.2 Ground Plane Currents	24
3.3 Analysis	29
3.4 Modified Designs	34
3.5 Conclusions	37
CHAPTER 4 A CIRCUIT MODEL FOR ANTENNA SYSTEMS WITH GROUND PLANE SLOTS	38
4.1 Transmission-Line Model	38
4.2 Self and Mutual Admittance Calculation	51
4.3 Results	54
4.4 Analysis	55
4.5 Conclusions	59
CHAPTER 5 A NOVEL GROUND PLANE SLOT DESIGN	60
5.1 Mustache Design Concept	60
5.2 Sample Design for H-Plane Configuration	62

5.2.1 Results	64
5.3 Conclusions	67
CHAPTER 6 CONCLUSIONS	68
REFERENCES	71
AUTHOR'S BIOGRAPHY	73

LIST OF FIGURES

1.1	Ground plane slot design by Chiu et al. [4].	3
1.2	Measured S-parameters reported by Chiu et al. [4].	3
1.3	Ground plane slot design by Alvey [5].	4
1.4	Simulated and measured S-parameters reported by Alvey [5].	4
1.5	Ground plane slot design by Eswarappa et al. [6].	5
2.1	Ground plane slot design by Chiu et al. [4].	6
2.2	Ground plane slot design by Alvey [5].	7
2.3	Enlarged view of Alvey meander-line block design [5].	7
2.4	Simulated S_{11} (orange) and S_{21} (blue) from HFSS models of Chiu slot design (dashed line) and Chiu base configuration (solid line).	8
2.5	Simulated S_{11} (orange) and S_{21} (blue) from HFSS model of Alvey slot design (dashed line) and Alvey base configuration (solid line).	9
2.6	Base design for Comparison Case 1: $\epsilon_r = 2.2$, $f_0 = 2.37$ GHz, substrate thickness 1.575 mm.	10
2.7	Base design for Comparison Case 2: $\epsilon_r = 4.6$, $f_0 = 0.925$ GHz, substrate thickness 1.6 mm.	11
2.8	Implementation of Alvey design for Comparison Case 1: $\epsilon_r =$ 2.2 , $f_0 = 2.37$ GHz, substrate thickness 1.575 mm. Element width 6.1 mm, line width 0.5 mm, gap width and interele- ment spacing 0.3 mm, element length 6.2 mm.	12
2.9	Implementation of Chiu design for Comparison Case 1: $\epsilon_r =$ 2.2 , $f_0 = 2.37$ GHz, substrate thickness 1.575 mm.	13
2.10	Simulated S-parameters for Case 1: base case (dashed line), Alvey design (solid line), and Chiu design (dotted line).	15
2.11	E-plane co-polar realized gain (in dB) of Comparison Case 1 base, Alvey, and scaled Chiu designs (simulated results from Ansoft HFSS).	16
2.12	H-plane co-polar realized gain (in dB) of Comparison Case 1 base, Alvey, and scaled Chiu designs (simulated results from Ansoft HFSS).	16

2.13	E-plane cross-polar realized gain (in dB) of Comparison Case 1 base, Alvey, and scaled Chiu designs (simulated results from Ansoft HFSS).	17
2.14	H-plane cross-polar realized gain (in dB) of Comparison Case 1 base, Alvey, and scaled Chiu designs (simulated results from Ansoft HFSS).	17
3.1	E-plane base configuration. Substrate height = 1.575 mm, $\epsilon_r = 2.2$, $f_0 = 2.38$ GHz, ground plane width = 83 mm.	20
3.2	H-plane base configuration. Substrate height = 1.575 mm, $\epsilon_r = 2.2$, $f_0 = 2.38$ GHz. Ground plane x dimension nominally 83 mm, can be varied.	21
3.3	Ground plane slot design by Chiu et al. [4].	21
3.4	Response of Chiu slot design to slot scaling when implemented on E-plane base configuration.	22
3.5	Response of Chiu slot design to changes in slot length when implemented on H-plane base configuration with slot width = 1.5 mm and slot spacing = 2 mm, showing slot dip remains fixed in frequency when slot length is changed.	23
3.6	Response of Chiu slot design to changes in slot length when implemented on H-plane base configuration with ground plane width = 53 mm, slot width = 2 mm, and slot spacing = 2.5 mm. Circled peaks are linked to independent slot mode, shift in frequency as slot length changes.	23
3.7	Ground plane slot design by Alvey [5].	24
3.8	Enlarged view of Alvey meander-line block design [5].	25
3.9	Simulated S_{21} (dB) of two-antenna system in E-plane configuration with Alvey slot design y dimension held constant, x dimension (L) varied. Slot-induced features move up in frequency as L decreases.	25
3.10	S-parameters of two-antenna system in H-plane configuration with Alvey slot design and without slots (base configuration).	26
3.11	Simulated vector current on ground plane of original Chiu slot design, antennas in H-plane configuration (left antenna active, results from Ansoft HFSS).	26
3.12	Simulated electric field in slots of original Chiu slot design, antennas in H-plane configuration (left antenna active, results from Ansoft HFSS).	27
3.13	Simulated vector current on ground plane of scaled Chiu slot design, antennas in E-plane configuration (left antenna active, results from Ansoft HFSS).	28

3.14	Simulated electric field in slots of scaled Chiu slot design, antennas in E-plane configuration (right antenna active, results from Ansoft HFSS).	28
3.15	Simulated surface current magnitude on ground plane of original Alvey design (E-plane configuration, left antenna active, results from Ansoft HFSS).	30
3.16	Simulated surface current magnitude on ground plane of Alvey design with antennas in H-plane orientation (left antenna active, results from Ansoft HFSS).	30
3.17	Enlarged view of rotated meander-line block design tested in H-plane configuration.	31
3.18	Simulated surface current magnitude on ground plane of Alvey design with meander-line blocks rotated by 90°, H-plane configuration (left antenna active, results from Ansoft HFSS).	31
3.19	Simulated surface current magnitude on ground plane of modified Alvey design with a gap in the center of the row of meander-line blocks (H-plane configuration, left antenna active, results from Ansoft HFSS).	32
3.20	Simulated S-parameters for scaled Chiu design with varying ground plane width. Slot length = 28 mm, slot width = 1.5 mm, and slot spacing = 2 mm (results from Ansoft HFSS).	33
3.21	S-parameters for Chiu design operating in dipole mode with ground plane width = 53 mm, slot width = 1.5 mm, slot spacing = 2 mm, and slot length = 25 mm (results from Ansoft HFSS).	35
3.22	S-parameters for H-plane configuration Alvey design with center gap and varying ground plane width (results from Ansoft HFSS).	36
4.1	Problem geometry: two microstrip patch antennas with a shared ground plane which contains some slot structure. Electric fringing field along patches' edges is modeled as electric field in slots (areas with diagonal lines) for the purpose of self and mutual admittance calculations.	39
4.2	Transmission line model of two-antenna system including coupling from ground plane slot structure.	40
4.3	Definition of voltage for mutual admittance calculation to agree with circuit model.	41
4.4	Antennas closely spaced and arranged in a line along their E-planes, which can be approximated with a simpler circuit model.	42

4.5	Simplified transmission line model for closely spaced E-plane oriented configuration. Antenna 2, not pictured, is a mirror image of Antenna 1 (with appropriate substitution of component values).	42
4.6	H-plane configuration geometry with radiating edge effective slots modified into U shape that includes nonradiating edges' field distribution.	43
4.7	Transmission line model of two-antenna system including coupling from ground plane slot structure and slot port definitions for circuit analysis.	44
4.8	Diagram of the connection between Port 1, Slot 1, and Slot 2, including voltage and current definitions.	46
4.9	Two-port network including all mutual coupling in the simplified E-plane model.	49
4.10	Real and imaginary parts of self-admittance of a 61 mm slot dipole as calculated from [16] (solid lines) and using Babinet's principle with the self-impedance of a cylindrical dipole, from [19].	55
4.11	Calculated S-parameters for scaled Chiu slot structure implemented on E-plane oriented base configuration, compared to calculated base configuration S-parameters and simulated results for the same models.	56
4.12	Transmission line model for single patch antenna, including coupling between edge slots.	57
4.13	Dependent current sources on one radiating edge of one patch in the presence of ground plane slots and a second antenna.	57
5.1	Mustache ground plane slot design on H-plane base system configuration.	63
5.2	Simulated S_{21} for H-plane base configuration, symmetric mustache slot structure, and asymmetric mustache slot structure (simulated results from Ansoft HFSS).	64
5.3	E-plane realized co-polar gain (in dB) of H-plane base configuration (black line) and systems with symmetric and asymmetric mustache slot structures (blue and orange lines, respectively), (simulated results from Ansoft HFSS).	65
5.4	H-plane realized co-polar gain (in dB) of H-plane base configuration (black line) and systems with symmetric and asymmetric mustache slot structures (blue and orange lines, respectively), (simulated results from Ansoft HFSS).	65

5.5	E-plane realized cross-polar gain (in dB) of H-plane base configuration (black line) and systems with symmetric and asymmetric mustache slot structures (blue and orange lines, respectively), (simulated results from Ansoft HFSS).	66
5.6	H-plane realized cross-polar gain (in dB) of H-plane base configuration (black line) and systems with symmetric and asymmetric mustache slot structures (blue and orange lines, respectively), (simulated results from Ansoft HFSS).	66
5.7	Measured S_{21} for H-plane base configuration, symmetric mustache slot design, and asymmetric mustache slot design.	67

CHAPTER 1

INTRODUCTION AND BACKGROUND

1.1 Introduction

When two or more antennas are located near one another, mutual coupling can occur between them. This can result in degradation of their radiation patterns and changes in input impedance. In arrays, mutual coupling can cause enough impedance mismatch to cause blind angles. Alternatively, if the antennas are not part of the same system, their coupling may cause the two systems to receive unwanted signals from one another.

The simplest methods for reducing coupling between adjacent antennas are moving the antennas further apart and orienting them so that their polarizations are mismatched [1]. Often the designer of an antenna has no control over its placement, however, so those methods cannot usually be applied. What remains is to introduce some structure between the two coupled antennas that prevents or cancels their mutual excitation. Several such approaches have been reported, including electronic band gap structures [2], [3], resonant-size ground plane slot structures [4]–[6], and resonant slot-coupled cavities behind the ground plane [5].

In this work we investigate ground plane slot structures because, out of the reported approaches, they are the easiest and least expensive to integrate into an existing system. Electronic band gap structures are very sensitive to manufacturing error and often require vias through the substrate, which add cost. A cavity behind the ground plane adds substantial weight and volume.

The ground plane slot designs have no vias, less intense manufacturing tolerances, and no added material, so they are quite promising as an approach to the mutual coupling problem. At present, however, no analytical model for the slots' interaction with nearby antennas has been reported, nor have any design guidelines for their implementation in new systems. For these reasons, this work examines ground plane slot structures in detail. The goal is to enable designers to implement slots in more complex situations, such as multiband or polarization-agile systems, by improving the theoretical understanding of slot structures and creating an accessible model for use in their design.

The remainder of this chapter will introduce the ground plane slot structures reported by Chiu et al., Eswarappa et al., and Alvey. The next chapter compares the performance and scalability of the Chiu and Alvey designs. In Chapter 3, we investigate the reported slot structures' excitation behavior. A circuit model that describes the slots' interaction with microstrip patch antennas will be introduced in Chapter 4. Finally the insights gained about excitation will be combined with the circuit model to develop a new slot design that is more flexible than those already reported.

1.2 Background: Reported Designs

In this work we use reported ground plane slot designs as clues to develop a broader understanding of their operation.

The design reported by Chiu et al. is shown in Figure 1.1. Ground plane slots were added to a two-antenna test configuration. The slots touch the edge of the ground plane and are cut toward the center, leaving a continuous strip connecting the ground plane on either side. While the slots were implemented in systems with several types of antennas, here we focus on their implementation

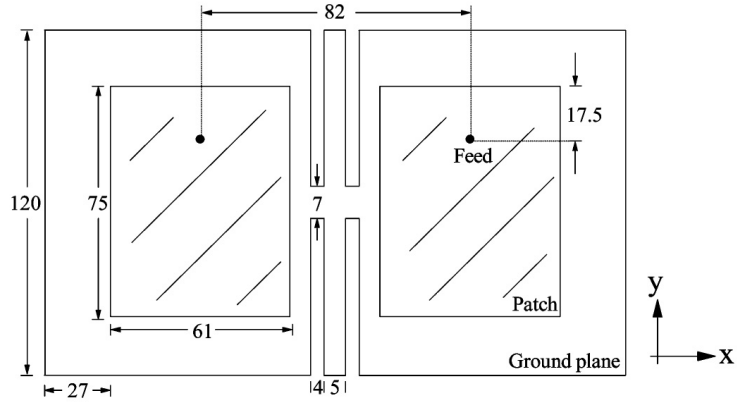


Figure 1.1: Ground plane slot design by Chiu et al. [4].

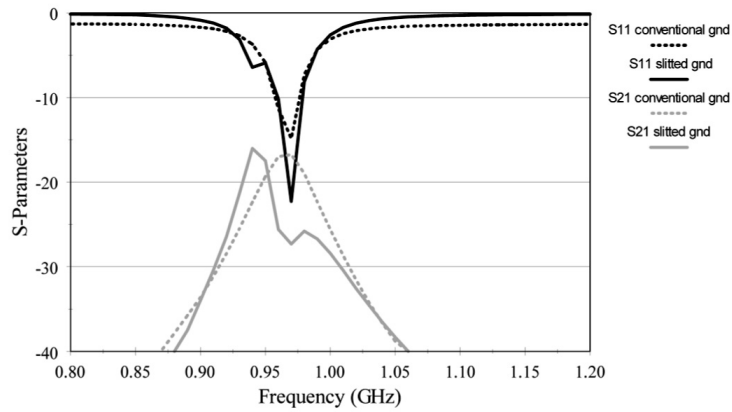


Figure 1.2: Measured S-parameters reported by Chiu et al. [4].

with microstrip patches. Measured S-parameters reported by Chiu, compared to a base design without slots, are shown in Figure 1.2 [4]. The reported design improved in-band isolation by 10.6 dB. The authors described their structure as a band-stop filter and illustrated this by fabricating a microstrip-fed version [4].

Figure 1.3 shows the design reported by Alvey. In this case, interlacing slots create a series of meander-line blocks in the center of the ground plane between two patch antennas. The path length of the meander line in each block is approximately an effective half wavelength. Simulated and measured S-parameters reported by Alvey, compared to a base design without slots, are

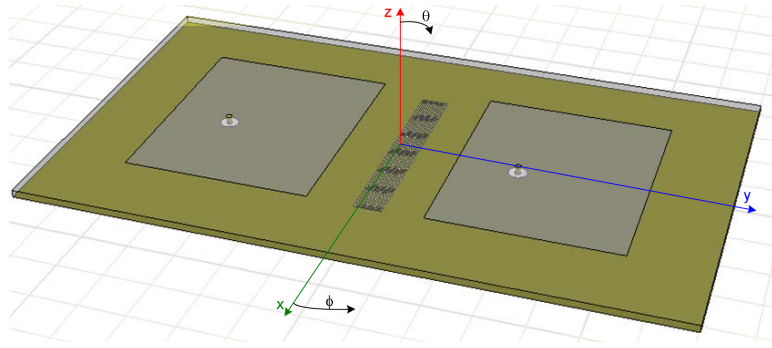


Figure 1.3: Ground plane slot design by Alvey [5].

shown in Figure 1.4. The Alvey slot structure results are labeled “FSS” because the author believed the slots might be acting as a frequency selective surface.

This design improved in-band isolation by approximately 5 dB.

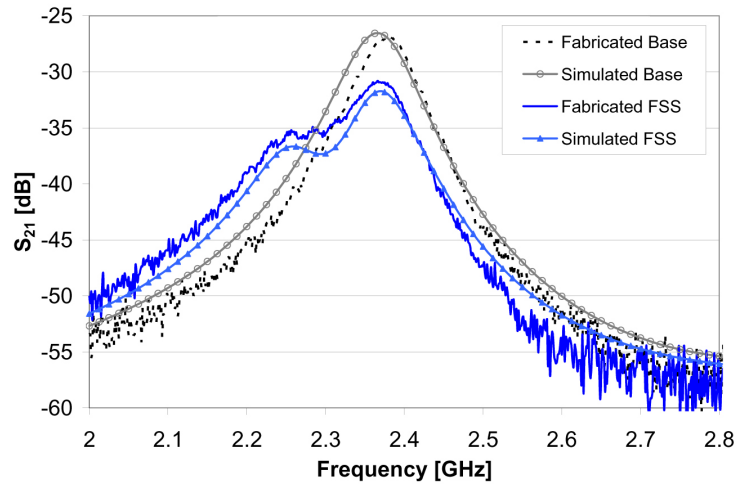


Figure 1.4: Simulated and measured S-parameters reported by Alvey [5].

In [6], Eswarappa et al. use a periodic grid of resonant-size circles etched in the ground plane (Figure 1.5) to isolate transmit and receive arrays. The circles’ resonant dimensions were comparable to those of the patches in the array. Thus the ground plane between the two arrays was etched with circles, rather than the ground plane between individual antennas. Additionally, to prevent

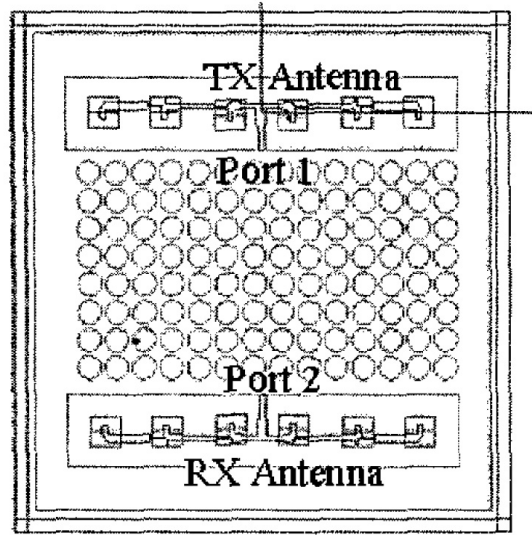


Figure 1.5: Ground plane slot design by Eswarappa et al. [6].

radiation into the back plane, the area with the etched circles was backed by a cavity. The group reported an isolation improvement between the two arrays of more than 15 dB. Since this design uses large slot structures that will not fit between individual antennas in a typical array with half-wavelength spacing, it does not lend itself to direct comparison with the other reported slot designs. For the rest of this work we focus on the Chiu and Alvey designs.

CHAPTER 2

COMPARISON OF REPORTED GROUND PLANE SLOT STRUCTURES

2.1 Designs for Comparison

This chapter compares the behavior of the ground plane slot designs by Chiu et al. [4] and Alvey [5]. The reported designs were introduced in Chapter 1 and are repeated for convenience in Figures 2.1 and 2.2, respectively. Measured S-parameters reported by Chiu, compared to a base design without slots, were shown in Figure 1.2. The reported design improved in-band isolation by 10.6 dB. Simulated and measured S-parameters reported by Alvey, compared to a base design without slots, were shown in Figure 1.4. This design improved in-band isolation by approximately 5 dB. An enlarged view of one meander-line block is shown in Figure 2.3.

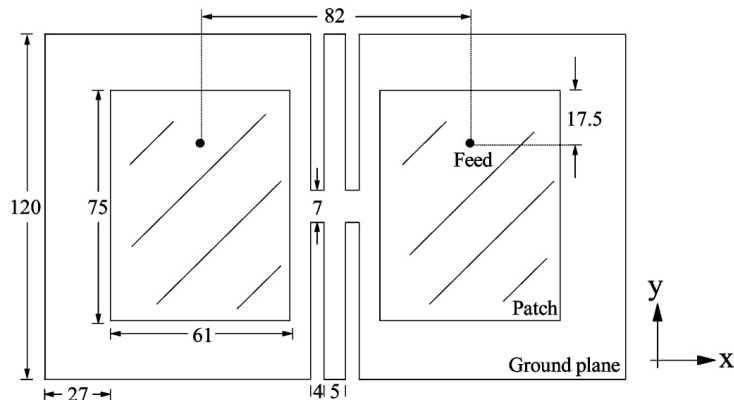


Figure 2.1: Ground plane slot design by Chiu et al. [4].

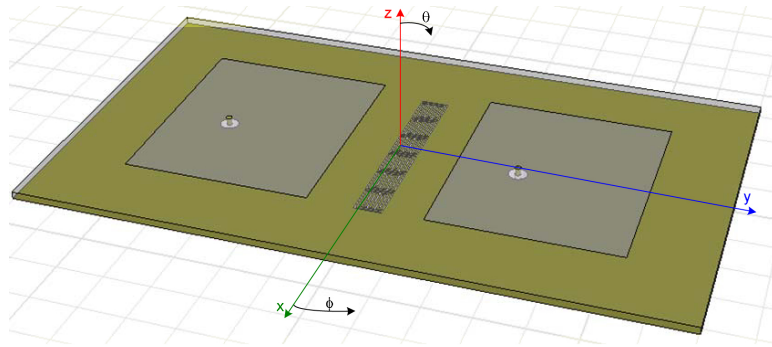


Figure 2.2: Ground plane slot design by Alvey [5].

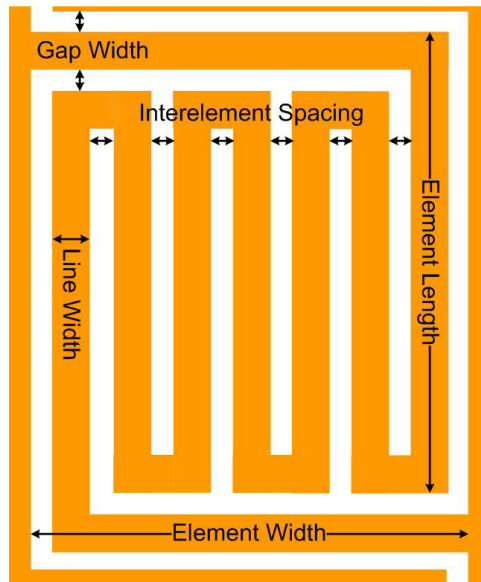


Figure 2.3: Enlarged view of Alvey meander-line block design [5].

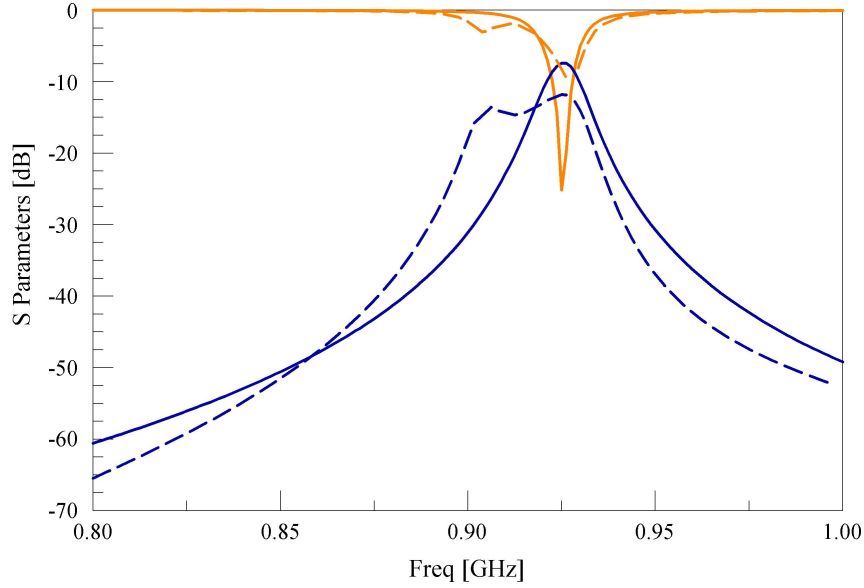


Figure 2.4: Simulated S_{11} (orange) and S_{21} (blue) from HFSS models of Chiu slot design (dashed line) and Chiu base configuration (solid line).

First, the two ground plane slot structures were simulated to ensure that their behavior could be duplicated in Ansoft HFSS [7]. The location of the probe feeds in the Chiu design had to be shifted toward the antenna centers by 10.75 mm to achieve a good impedance match, but the original designs are otherwise unchanged. Simulation results from the HFSS model of the Chiu design are shown in Figure 2.4. Simulation results from the HFSS model of the Alvey design are shown in Figure 2.5.

2.2 Base Configuration Design Discussion

Since the Chiu and Alvey designs operate at different frequencies on different substrates, it is difficult to directly compare their behavior. Two different comparison cases were designed in order to be able to compare “apples to apples.” In Comparison Case 1, the Alvey and Chiu designs are both implemented on a base design which operates using the same frequency, antenna

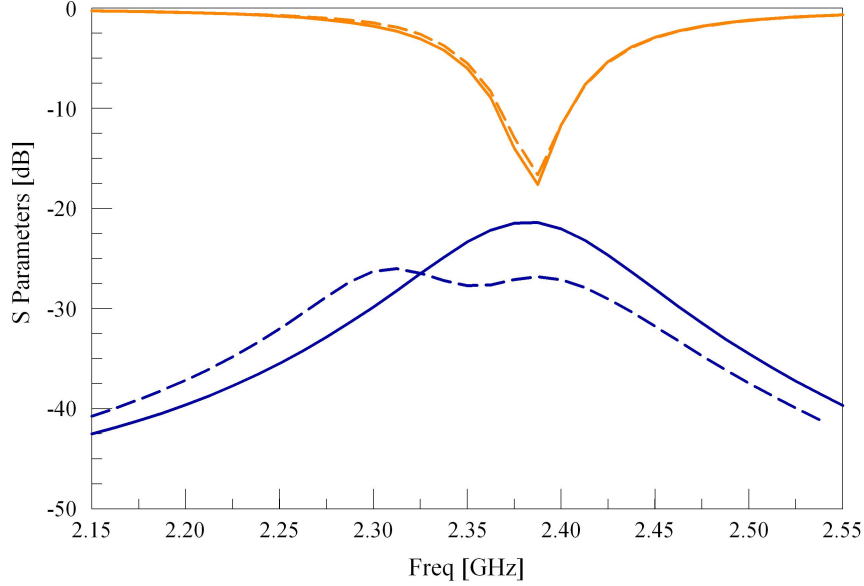


Figure 2.5: Simulated S_{11} (orange) and S_{21} (blue) from HFSS model of Alvey slot design (dashed line) and Alvey base configuration (solid line).

dimensions, and substrate as the original Alvey design. In Comparison Case 2, the base design operates using the frequency, antenna dimensions, and substrate of the Chiu design. Thus in Case 1 the Chiu design must be modified, and in Case 2 the Alvey design must be modified.

The original Chiu and Alvey designs also have different antenna orientations. In the Chiu design, the two antennas are arranged in a line along their H-planes, while in the Alvey design they are lined up along their E-planes. In order that the two comparisons be consistent with one another, we will choose the same antenna orientation for both comparison cases. According to Jedlicka et al. [8], space-wave coupling is strongest in the E-plane of microstrip patch antennas. Haddad and Pozar [9] report that patch antennas launch a surface wave mode in the E-plane that decays as $\rho^{-1/2}$, while the lowest-order mode in the H-plane decays as $\rho^{-3/2}$. Therefore higher surface wave coupling is also expected in the E-plane. Based on this evidence, arranging the antennas along a line in their

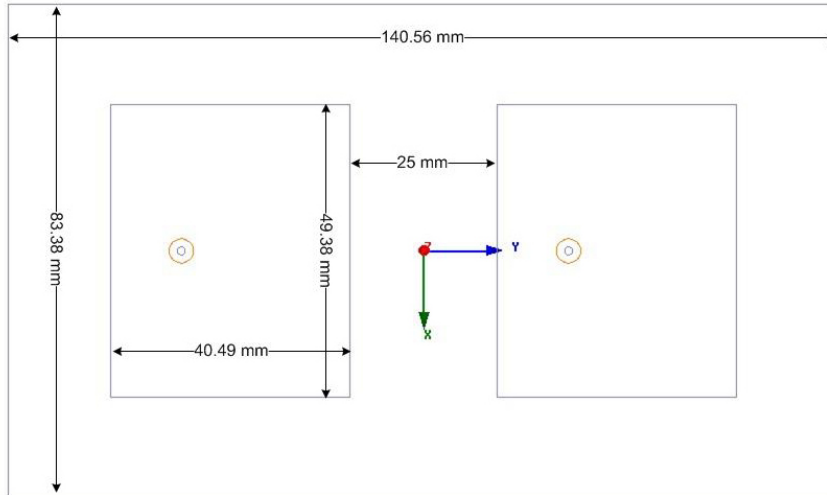


Figure 2.6: Base design for Comparison Case 1: $\epsilon_r = 2.2$, $f_0 = 2.37$ GHz, substrate thickness 1.575 mm.

E-planes should cause the most coupling in the base case. In order to most effectively test the isolation improvement provided by the two ground plane slot structures in a “worst-case” scenario, the antennas will therefore be aligned along their E-planes in both comparison cases.

The base design for Comparison Case 1 is shown in Figure 2.6. The dimensions are identical to those of the Alvey base design.

The base design for Comparison Case 2 is shown in Figure 2.7. The antenna dimensions and edge-to-edge spacing are identical to those of the original Chiu design, but the antennas are rotated so that they are collinear in the E-plane. In order to preserve the dimensions of the Chiu slot structure, the ground plane x dimension is not changed. The ground plane y dimension is increased to accommodate the new antenna orientation, preserving the space from the antenna edge to the ground plane edge.

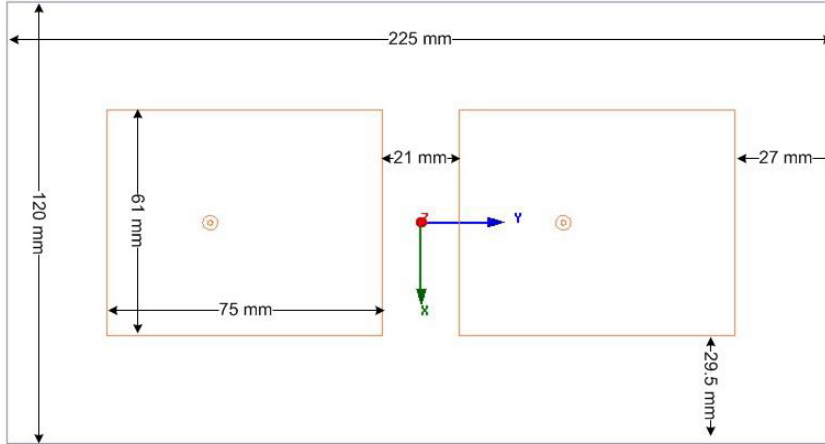


Figure 2.7: Base design for Comparison Case 2: $\epsilon_r = 4.6$, $f_0 = 0.925$ GHz, substrate thickness 1.6 mm.

2.3 Ground Plane Slot Design Scaling

Since the ground plane slots are not backed by another conductor, they are subject to a different effective dielectric constant than the patch antennas, whose resonant cavities are largely contained within the substrate. The effective dielectric constant is not simply ϵ_r of the substrate, but instead a weighted average of the substrate dielectric constant with that of the surrounding air. When a slot structure is scaled to operate in a different system than it was originally designed for, the relationship shown in Equation (2.1) is used to approximate the relationship between the slot structure's effective wavelengths in the old and new systems. The effective wavelength of the second design, denoted $\lambda_{\text{eff}2}$, is related to that of the original design, $\lambda_{\text{eff}1}$, by this ratio. Thus, given a small amount of knowledge about the resonant behavior of the slots, we can scale them to the right size relative to the new effective wavelength.

$$\frac{\lambda_{\text{eff}2}}{\lambda_{\text{eff}1}} = \frac{f_1}{f_2} \sqrt{\frac{w_1 \epsilon_1 + (1 - w_1)}{w_2 \epsilon_2 + (1 - w_2)}} \quad (2.1)$$

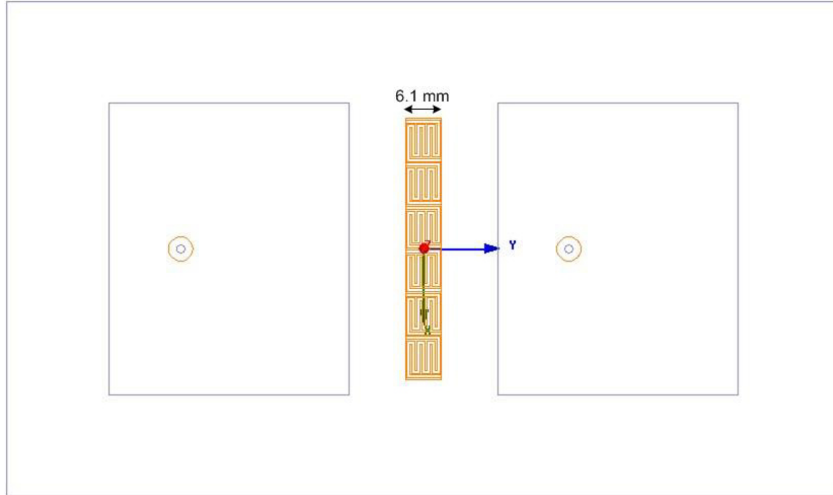


Figure 2.8: Implementation of Alvey design for Comparison Case 1: $\epsilon_r = 2.2$, $f_0 = 2.37$ GHz, substrate thickness 1.575 mm. Element width 6.1 mm, line width 0.5 mm, gap width and interelement spacing 0.3 mm, element length 6.2 mm.

The weighting functions w_1 and w_2 depend on the electrical thickness of the dielectric and the width of the slots. If the dielectric fills an entire half space, the weighting function is $1/2$. Since the substrate is not infinitely thick, w_1 and w_2 are less than $1/2$. For many applications it is acceptable to assume a weight of $1/2$, but very thin substrates or high dielectric constants may show noticeable inaccuracy [10]. The effective wavelength can also be calculated using expressions for the characteristic properties of stripline in certain circumstances, but for highly convoluted structures like the Alvey design this may not be accurate. In certain cases, it is simpler to treat w_1 and w_2 as unknowns and look for scaling solutions within the possible range of $\lambda_{\text{eff}2}$ values.

In Case 1, the slots for the Alvey design are implemented on the base design without changes (Figure 2.8). In order to scale the Chiu slot design for the Case 1 base configuration, we first examine the original design. As will be discussed in more depth in the next chapter, the Chiu slot structure resonates across the width of the ground plane, so we know that the original design's ground plane

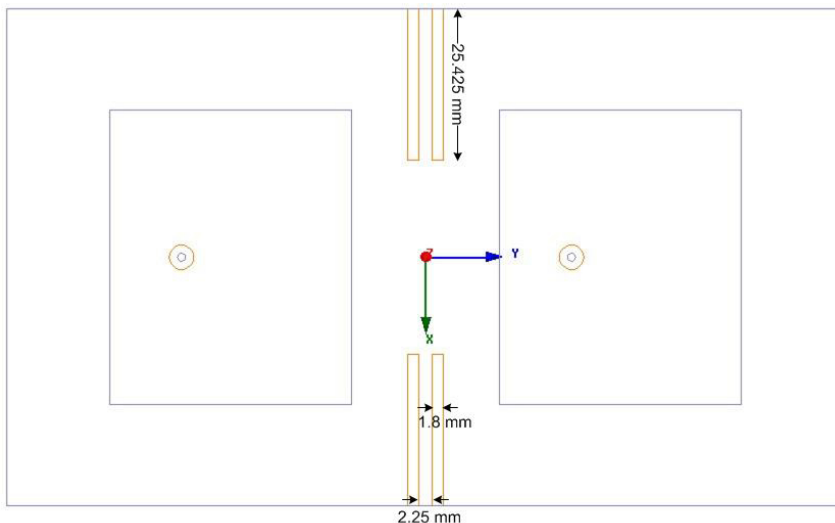


Figure 2.9: Implementation of Chiu design for Comparison Case 1: $\epsilon_r = 2.2$, $f_0 = 2.37$ GHz, substrate thickness 1.575 mm.

width (120 mm) is approximately one half of an effective wavelength. From Equation (2.1), we calculate that with weighting functions between 0 (free space) and 1/2 (dielectric filling an entire half space), the effective wavelength for slots on the Case 1 base configuration could be between 126 cm and 100 mm. In general a weighting function closer to 0.5 is most accurate, which would mean the Chiu slot structure should be scaled by a factor of $100 \text{ mm}/240 \text{ mm} = 0.42$. Experimentation with scaling factors near 0.42 showed that the best performance was obtained with a scaling factor of 0.43. Therefore, for Case 1 the Chiu design slots' length, width, and separation in the y direction are scaled by a factor of 0.43. Their separation in the x direction does not follow this scaling factor because the slots are required to touch the edges of the substrate. The scaled Chiu design is shown in Figure 2.9.

In Case 2, the Chiu design is implemented without scaling and works as expected. However, we were unable to create a working scaled version of the Alvey slot structure for this system configuration. This may be due to the

antennas' smaller spacing: closer proximity means that each antenna experiences more capacitance due to mutual coupling. Although narrower line widths and additional windings of the meander line were attempted, the inductance achievable by the meander-line blocks was limited, and slot-induced dips in mutual coupling were only achievable well outside the operating band of the antennas.

2.4 Simulated Results and Comparison

The two ground plane slot designs were compared based on their success at isolating the two antennas. In addition, since by including the slot structures we are breaking the continuity of the ground plane, we expect that the inclusion of slots may cause additional undesired radiation. Therefore we also examine backplane and cross-polar radiation. Since no satisfactory Alvey structure implementation could be found for Case 2, only Case 1 will be included in this section.

2.4.1 Isolation

Simulated S-parameters for the Case 1 base, Chiu, and Alvey designs are presented in Figure 2.10. Unsurprisingly, the Alvey design does function as expected and improve isolation, since it is unchanged from the original design. It reduces in-band coupling by 5.6 dB. The scaled Chiu design, due to the new antenna orientation, has a qualitatively different response from Chiu's reported design. However, the modified design still improves isolation, reducing in-band S_{21} by 5.4 dB compared to the original design's reported 10.6 dB reduction, and eliminating the out-of-band peak present in the response of the original design.

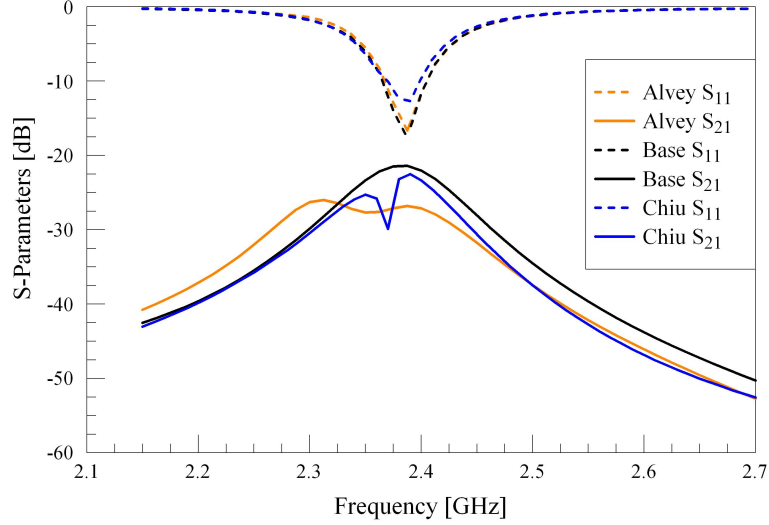


Figure 2.10: Simulated S-parameters for Case 1: base case (dashed line), Alvey design (solid line), and Chiu design (dotted line).

2.4.2 Undesired radiation

Because the designs introduce slots in the ground plane and modify the ground plane currents, undesired radiation is a concern. Figures 2.11 through 2.14 show the co-polar and cross-polar radiation patterns for Comparison Case 1 with both antennas active. The patterns of the Alvey, Chiu, and base designs are similar except for a few notable features. In the E-plane co-polar pattern (Figure 2.11), the Alvey and Chiu slot structures both increase backplane radiation, by about 7 dBi and 10.5 dBi respectively. In the H-plane co-polar pattern (Figure 2.12), we see the same increase in radiation directly backward, but the Alvey structure causes deep notches in the radiation pattern at $\theta = \pm 130^\circ$. The E-plane cross-polar levels of the Alvey and Chiu designs are uniformly higher than that of the base configuration (Figure 2.13). The three systems' H-plane cross-polar patterns (Figure 2.14) are virtually identical.

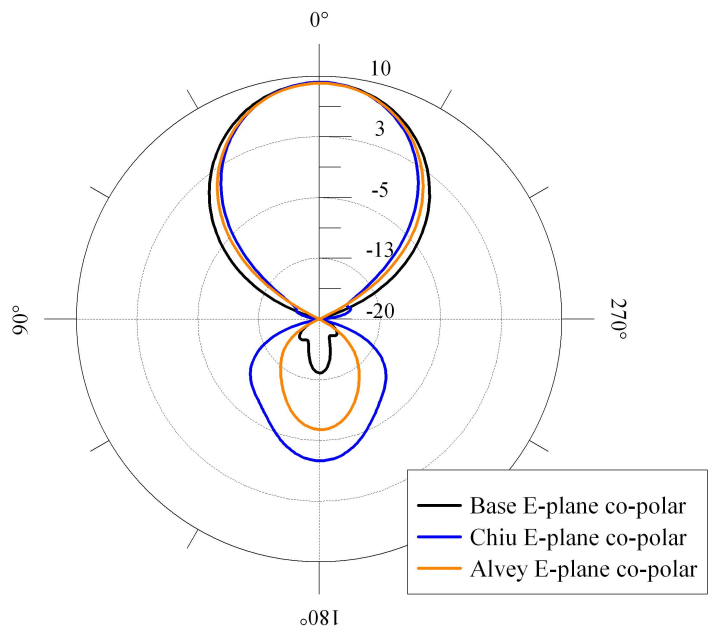


Figure 2.11: E-plane co-polar realized gain (in dB) of Comparison Case 1 base, Alvey, and scaled Chiu designs (simulated results from Ansoft HFSS).

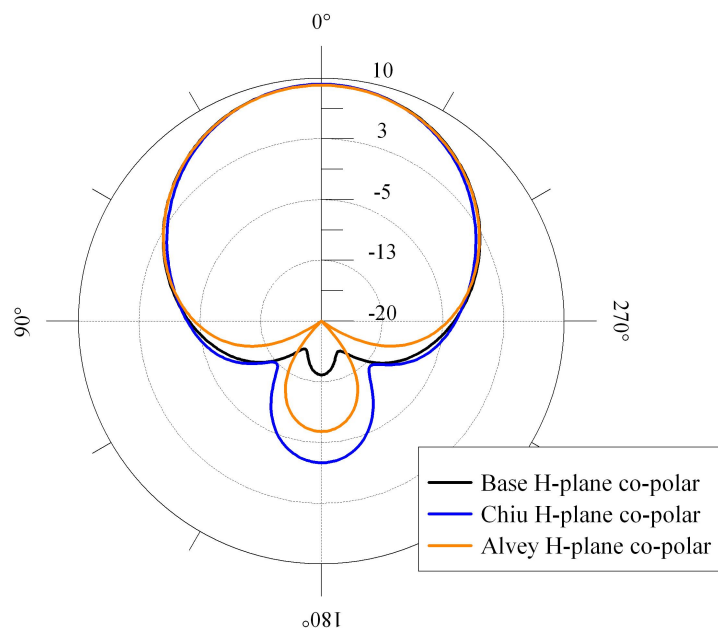


Figure 2.12: H-plane co-polar realized gain (in dB) of Comparison Case 1 base, Alvey, and scaled Chiu designs (simulated results from Ansoft HFSS).

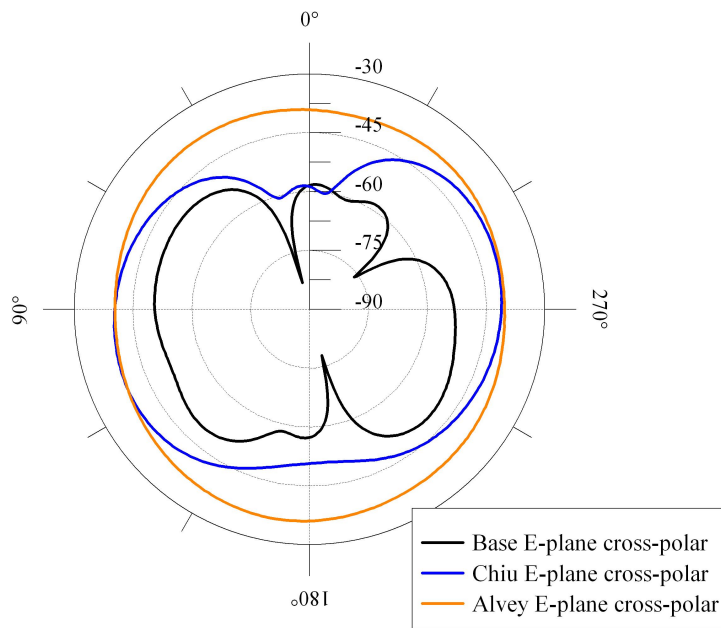


Figure 2.13: E-plane cross-polar realized gain (in dB) of Comparison Case 1 base, Alvey, and scaled Chiu designs (simulated results from Ansoft HFSS).

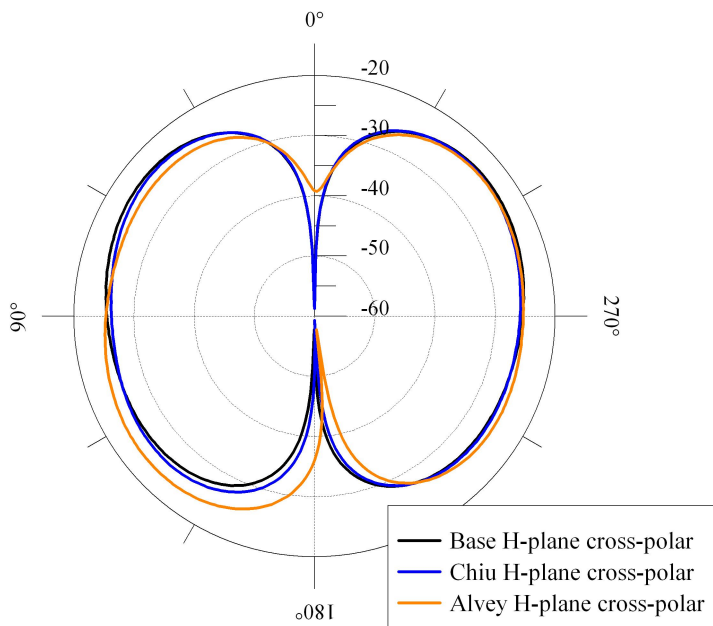


Figure 2.14: H-plane cross-polar realized gain (in dB) of Comparison Case 1 base, Alvey, and scaled Chiu designs (simulated results from Ansoft HFSS).

2.5 Conclusions

This chapter's comparison has determined that both reported designs are capable of reducing mutual coupling between adjacent antennas. The presence of either slot structure induced more cross-polarized radiation in the E-plane, and both slot structures increased backplane radiation (the Chiu structure more than the Alvey structure). The Alvey design could not be implemented on the Chiu base configuration, in which the edge-to-edge antenna spacing was much lower than in the Alvey base configuration, possibly because of the antennas' increased mutual capacitance. The Chiu design's response in the E-plane-oriented base configuration was qualitatively different than its response in its original, H-plane-oriented implementation. The design also requires that the slots touch the ground plane edge. These behaviors are related to the slots' excitation and will be examined further in the next chapter.

CHAPTER 3

INVESTIGATION OF GROUND PLANE SLOT STRUCTURE EXCITATION

In this chapter, we examine the excitation of ground plane slot isolation structures and its dependence on antenna orientation. The first section describes two example designs' frequency behavior as the slot structures are scaled with the antennas in both E-plane and H-plane orientations. Next, simulated data on ground plane current density is employed to provide more insight into the slot structures' excitation modes. An analytical investigation identifies the excitation modes and their dependence on the antennas' orientation. Finally, this information is employed to improve the performance of some of the designs from Section 3.1.

3.1 Initial Frequency Response to Scaling

In the course of scaling existing ground plane slot designs for the comparison in Chapter 2, it became clear that the slots' response to scaling was qualitatively different depending on the orientation of the antennas. In order to clarify the effect of the base configuration on ground plane slot excitation, several combinations of slot design and base configuration were investigated.

In every trial, the slot designs are implemented in a base system configuration consisting of two antennas sharing a substrate and ground plane. The previous chapter considered only one antenna orientation with respect to the slots. In this chapter we will consider two antenna orientations. When the

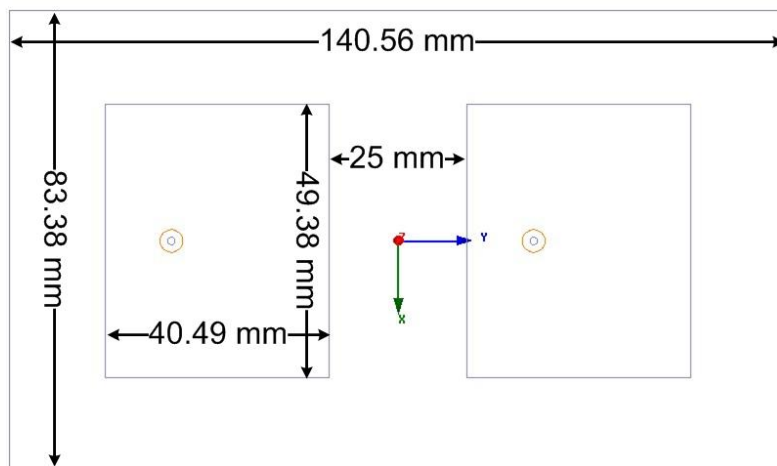


Figure 3.1: E-plane base configuration. Substrate height = 1.575 mm, $\epsilon_r = 2.2$, $f_0 = 2.38$ GHz, ground plane width = 83 mm.

antennas' E-planes are aligned (Figure 3.1), it will be referred to as the E-plane configuration, and when the antennas' H-planes are aligned (Figure 3.2), it will be referred to as the H-plane configuration. Both systems are implemented on a 1.575 mm thick substrate with $\epsilon_r = 2.2$ and the operating frequency is 2.38 GHz.

The slot design reported by Chiu et al. [4] is shown again in Figure 3.3. Scaling of this slot design was attempted with the antennas' H-planes aligned, as in the original design, and with their E-planes aligned (each antenna rotated 90° from its original orientation). When the antennas are implemented in the E-plane system configuration and the slots' length and width are scaled uniformly by a scaling factor, the features of the S_{21} plot induced by the slots shift in frequency as the scaling factor is modified (Figure 3.4). When the slots are implemented on the H-plane base configuration, some choices of slot

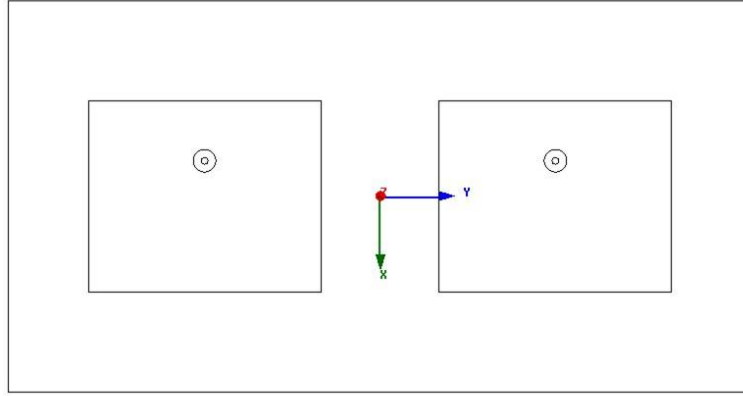


Figure 3.2: H-plane base configuration. Substrate height = 1.575 mm, $\epsilon_r = 2.2$, $f_0 = 2.38$ GHz. Ground plane x dimension nominally 83 mm, can be varied.

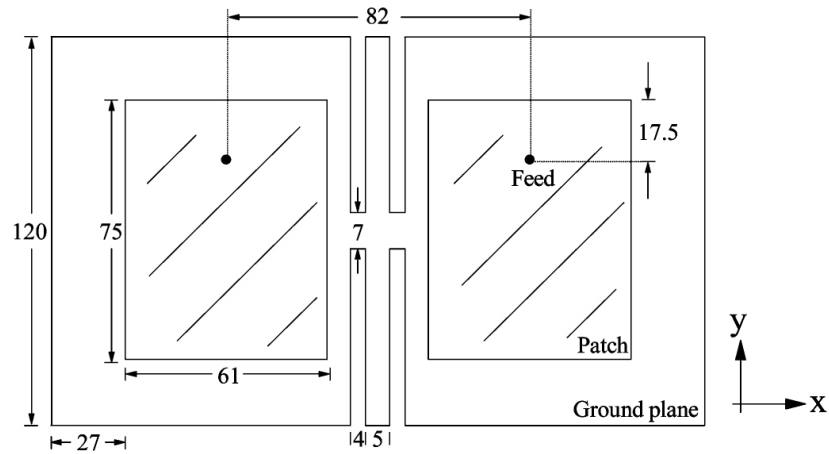


Figure 3.3: Ground plane slot design by Chiu et al. [4].

geometry result in a frequency response that does not shift with changes in slot length (Figure 3.5), and other choices of geometry result in a frequency response that does shift with changing slot length (Figure 3.6). The qualitative difference in frequency response leads to the expectation that this slot structure can support two different modes, one of which is only excitable in the H-plane orientation. The slot length appears to affect the frequency of the slot-induced features, while the slot width affects the magnitude of the slot-induced features. In the H-plane configuration, slot width also affects which mode is excited.

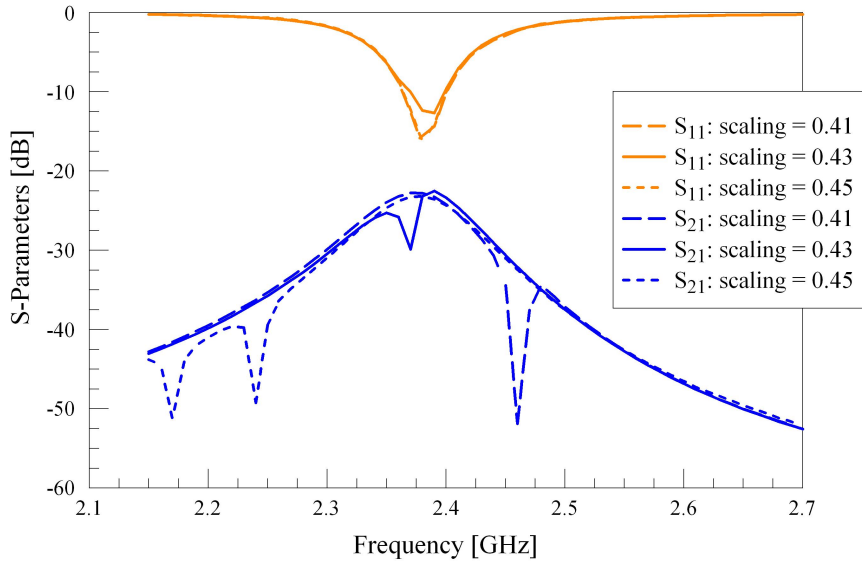


Figure 3.4: Response of Chiu slot design to slot scaling when implemented on E-plane base configuration.

The slot design reported by Alvey [5] is shown in Figure 3.7. An enlarged view of the meander-line block design is shown in Figure 3.8. The isolation improvement provided by this slot structure occurred when the total path length of the meander line was equal to an effective half wavelength at the system operating frequency. The path length was calculated by following a path directly along the center of the meandered trace, resulting in the expression given in

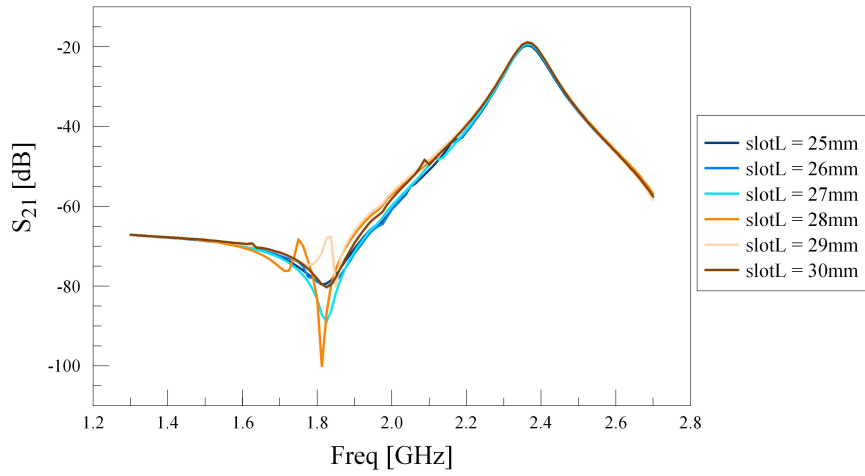


Figure 3.5: Response of Chiu slot design to changes in slot length when implemented on H-plane base configuration with slot width = 1.5 mm and slot spacing = 2 mm, showing slot dip remains fixed in frequency when slot length is changed.

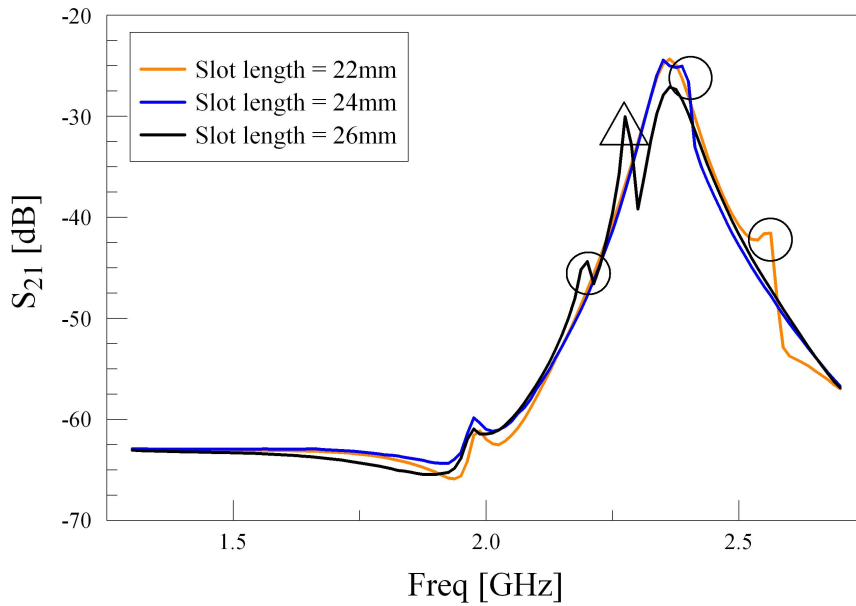


Figure 3.6: Response of Chiu slot design to changes in slot length when implemented on H-plane base configuration with ground plane width = 53 mm, slot width = 2 mm, and slot spacing = 2.5 mm. Circled peaks, which are linked to the independent slot mode, shift up in frequency as slot length decreases.

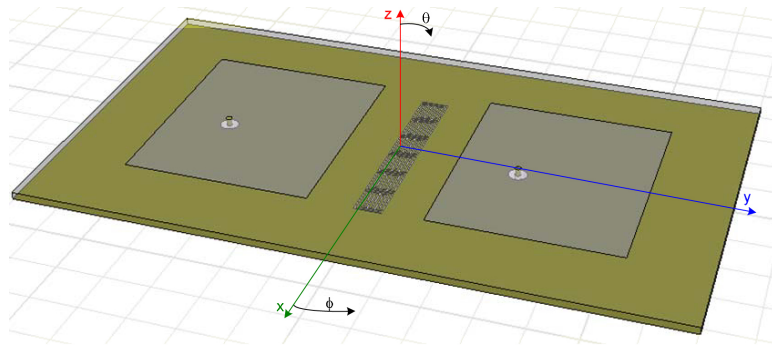


Figure 3.7: Ground plane slot design by Alvey [5].

Equation (3.1).

$$P = 3W + 7L - 9g - 14l \quad (3.1)$$

Above, W is the element width, L is the element length, g is the gap width, and l is the line width as shown in Figure 3.8. This slot design was simulated in a system configured with the antennas' E-planes aligned, as in the original design, and with their H-planes aligned (each antenna rotated 90° from its original orientation). When the antennas are in the E-plane orientation, the slots induce a small peak and adjacent dip in the S_{21} plot (Figure 3.9). However, when the antennas are in the H-plane orientation, no slot-induced features of S_{21} are apparent (Figure 3.10) [11].

3.2 Ground Plane Currents

The differences in behavior between the E-plane and H-plane imply that these two slot designs' excitation depends on the relative orientation and location of the antennas and slots. In order to gain more insight into the modes of excitation for each design, we examine the electric field in the slots and currents on the ground plane, both from simulation.

Ground plane currents and slot fields for the original Chiu design (in which

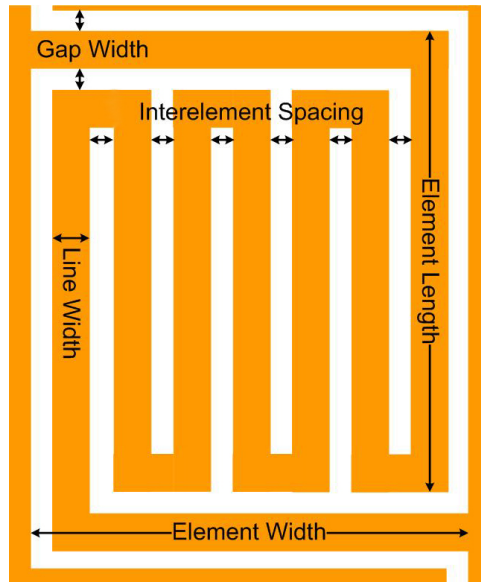


Figure 3.8: Enlarged view of Alvey meander-line block design [5].

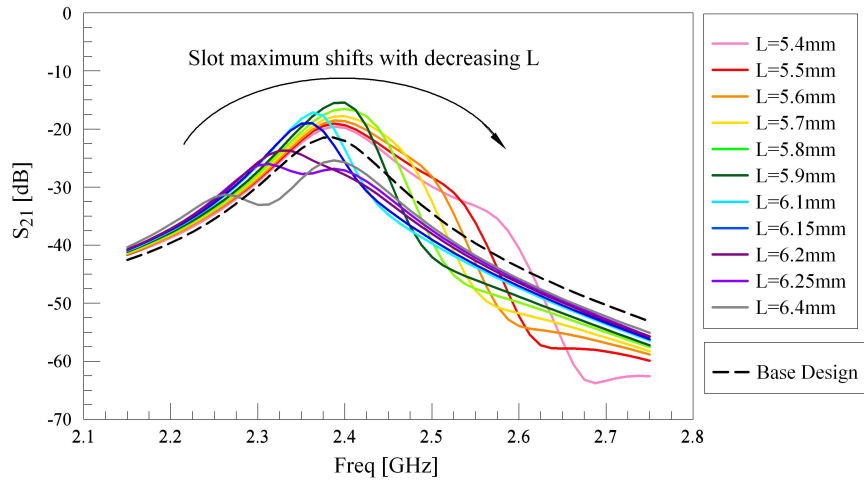


Figure 3.9: Simulated S_{21} (dB) of two-antenna system in E-plane configuration with Alvey slot design y dimension held constant, x dimension (L) varied. Slot-induced features move up in frequency as L decreases.

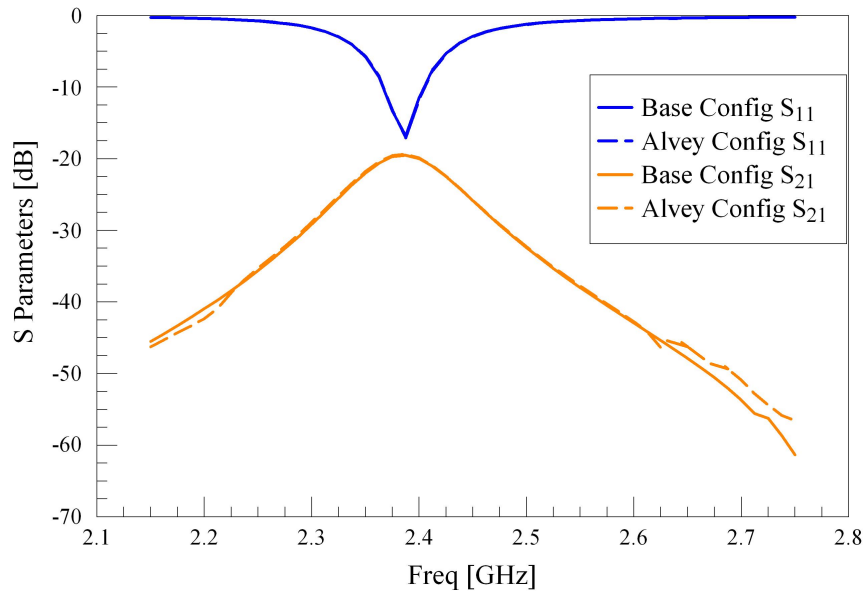


Figure 3.10: S-parameters of two-antenna system in H-plane configuration with Alvey slot design and without slots (base configuration).

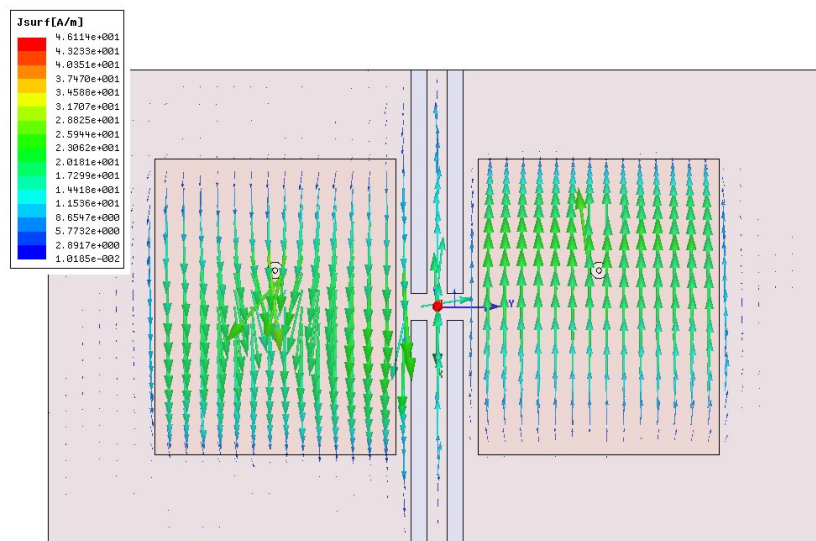


Figure 3.11: Simulated vector current on ground plane of original Chiu slot design, antennas in H-plane configuration (left antenna active, results from Ansoft HFSS).

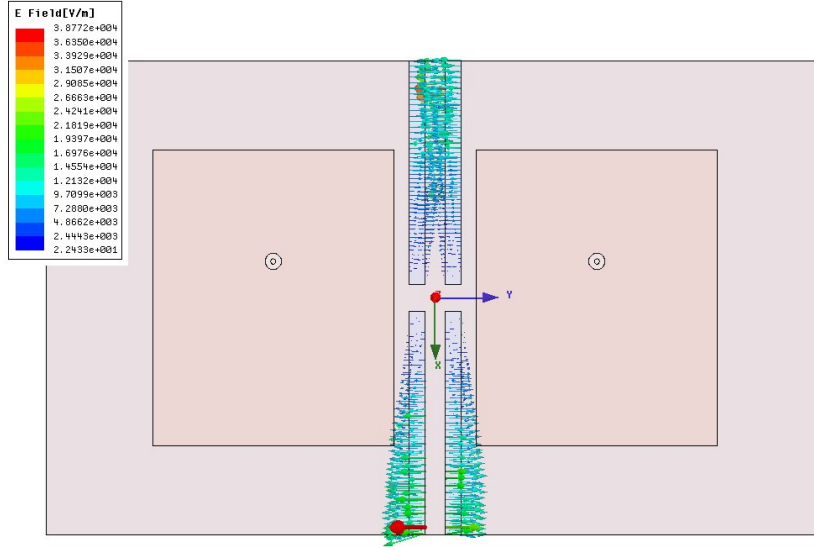


Figure 3.12: Simulated electric field in slots of original Chiu slot design, antennas in H-plane configuration (left antenna active, results from Ansoft HFSS).

the antennas are in the H-plane orientation) are shown in Figures 3.11 and 3.12, respectively. In these figures it is evident that there is a voltage difference across the width of the ground plane, since the current flows from one edge to the other and the electric field in the top pair of slots has opposite polarity from the field in the bottom pair. Ground plane currents and slot fields for a scaled, E-plane oriented configuration of the Chiu design are shown in Figures 3.13 and 3.14, respectively. In this case, the ground plane current and the electric field near the top pair of slots is the mirror image of that around the bottom pair of slots. Currents flow from each ground plane edge toward the center, and the electric field in the top and bottom slot pairs has the same polarity.

When considering the Alvey slot design, the most useful information is provided by a plot of the surface current magnitude on the ground plane. Figure 3.15 shows the original, E-plane oriented Alvey design's ground plane surface current density. The meander-line resonators are strongly excited by the active

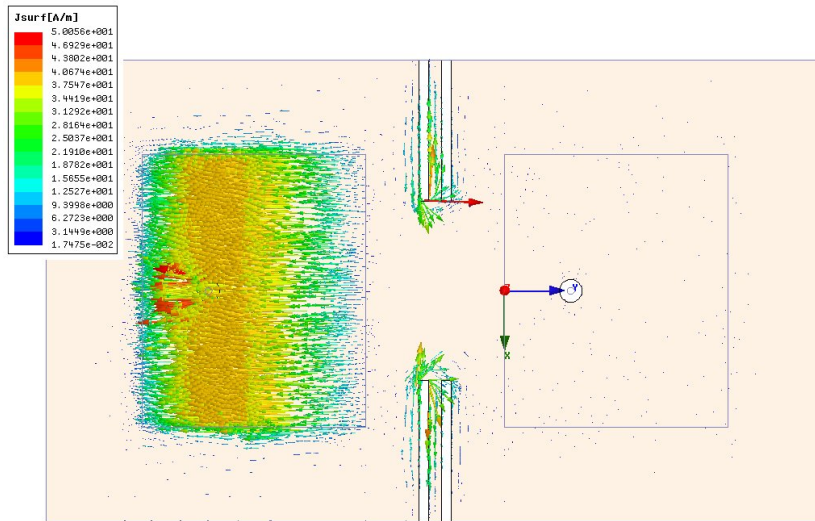


Figure 3.13: Simulated vector current on ground plane of scaled Chiu slot design, antennas in E-plane configuration (left antenna active, results from Ansoft HFSS).

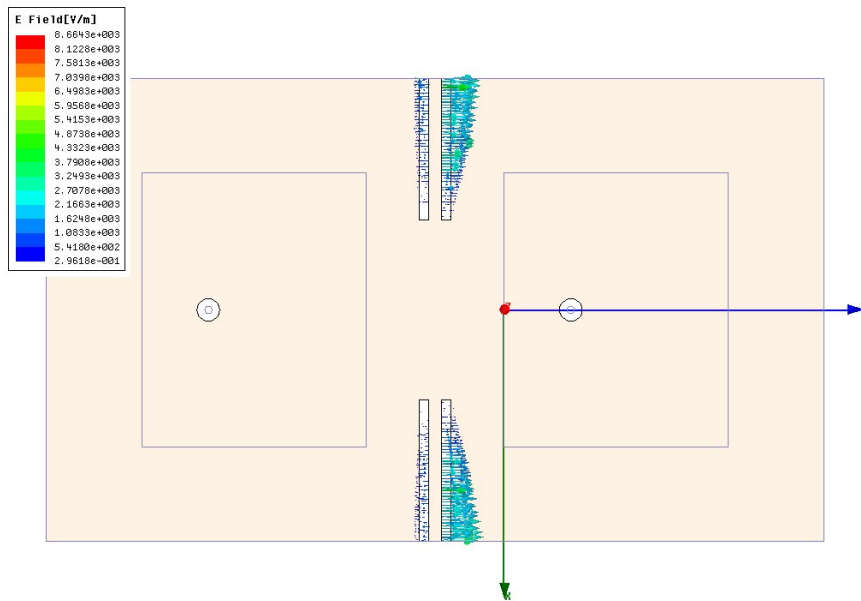


Figure 3.14: Simulated electric field in slots of scaled Chiu slot design, antennas in E-plane configuration (right antenna active, results from Ansoft HFSS).

antenna. When the antennas are in the H-plane orientation, the current density on the meander-line blocks is much lower (Figure 3.16), which agrees with the lack of slot effect in the S-parameter plot. In order to clarify the dependence of excitation on antenna orientation, a version of this design was simulated in which each meander-line block was rotated by 90° (shown close-up in Figure 3.17). This modified design exhibited negligible excitation of the meander-line blocks (Figure 3.18), implying that it is the adjacent radiating edge of the antenna that excites the meander-line blocks and not the direction of current on the patch. A third configuration using H-plane oriented antennas showed a promising response, however: when the row of meander-line blocks was split so that the ground plane was continuous at the center with meander line blocks touching each edge, plots of ground plane currents showed stronger excitation of the meander-line blocks (Figure 3.19). This improved response showed that placing the meander-line blocks in locations where the electric field fringing from the patches is stronger is a promising strategy for implementing the Alvey slots in an H-plane configuration, which will be further investigated in the next section.

3.3 Analysis

Using the effective dielectric constant discussed in Chapter 2, we find that in the original Chiu design the ground plane width is approximately a half wavelength at 0.97 GHz, in the operating band of the antenna. However, in the scaled configuration that produced Figure 3.5, the ground plane was near an effective half wavelength at 1.8 GHz while the operating frequency of the antenna was 2.38 GHz. This information on the electrical size of the design, together with the current and field plots presented earlier, leads to the conclusion that the H-plane orientation can excite a dipole-like mode in the Chiu slots. The opposite

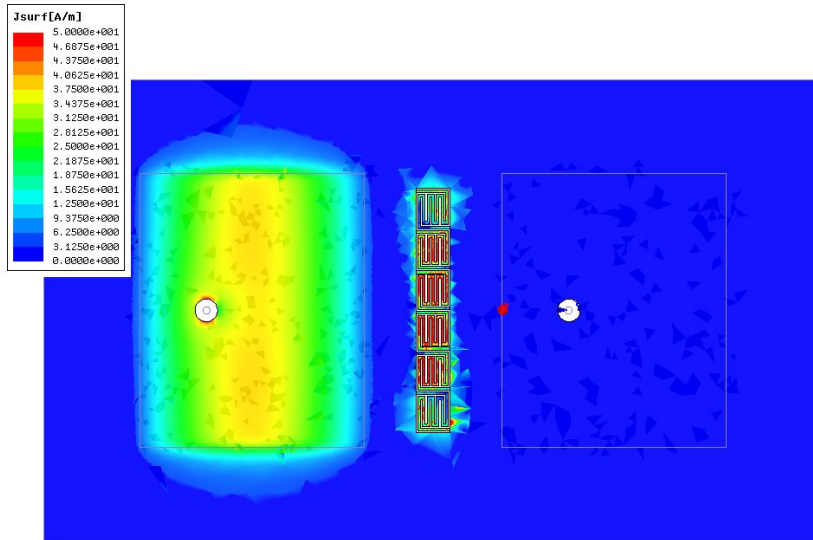


Figure 3.15: Simulated surface current magnitude on ground plane of original Alvey design (E-plane configuration, left antenna active, results from Ansoft HFSS).

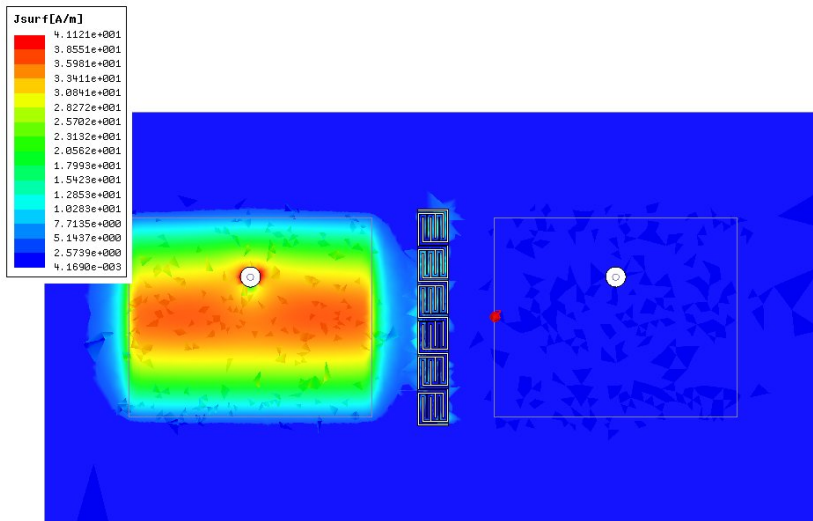


Figure 3.16: Simulated surface current magnitude on ground plane of Alvey design with antennas in H-plane orientation (left antenna active, results from Ansoft HFSS).

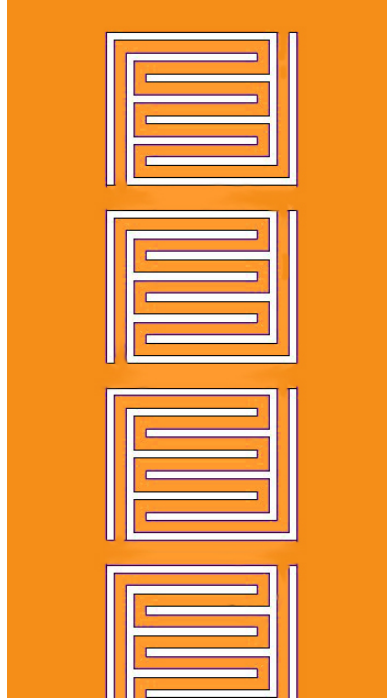


Figure 3.17: Enlarged view of rotated meander-line block design tested in H-plane configuration.

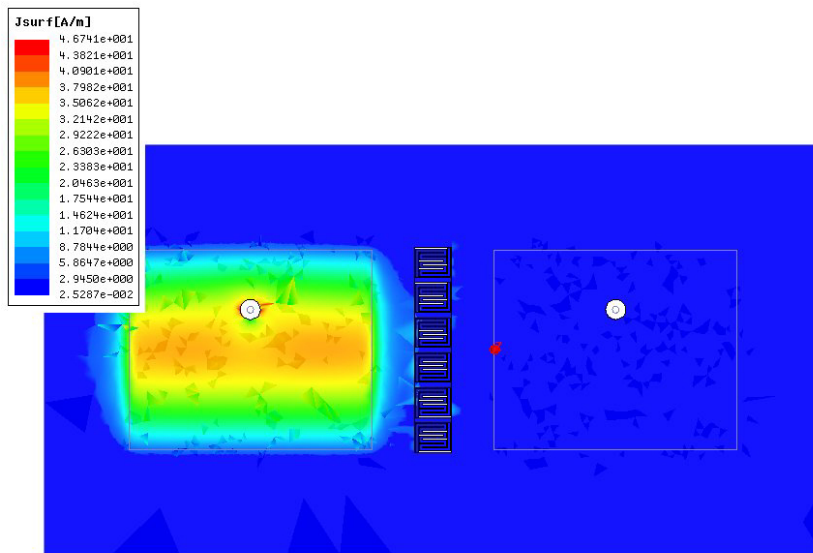


Figure 3.18: Simulated surface current magnitude on ground plane of Alvey design with meander-line blocks rotated by 90° , H-plane configuration (left antenna active, results from Ansoft HFSS).

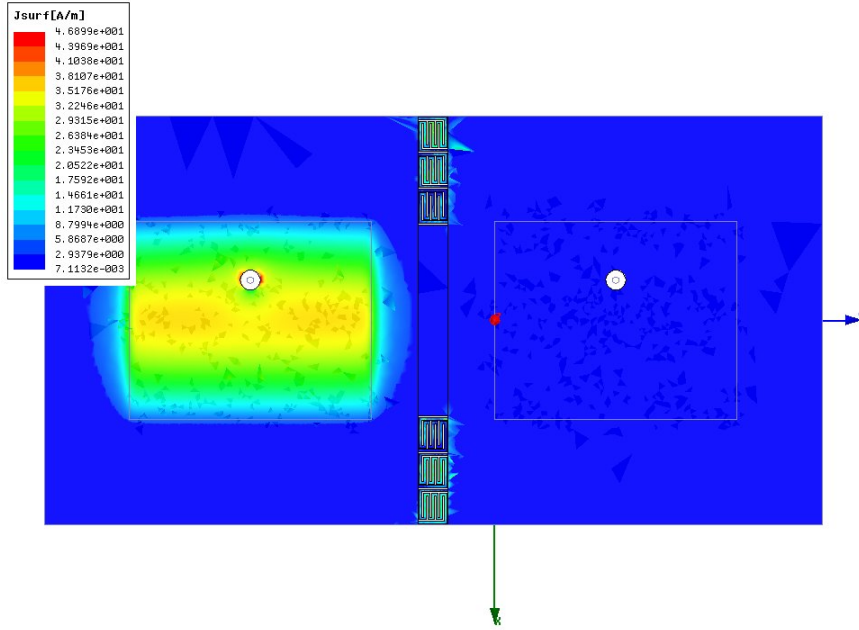


Figure 3.19: Simulated surface current magnitude on ground plane of modified Alvey design with a gap in the center of the row of meander-line blocks (H-plane configuration, left antenna active, results from Ansoft HFSS).

polarity between the top and bottom slot pairs follows the opposing polarity of the adjacent patch's fringing fields at the top and bottom edges. The behavior of this mode implies that for this mode to be excited, the ground plane size cannot be freely chosen - it is constrained by the effective wavelength for the slots. Because of that, if this configuration is implemented on a substrate with a relatively low dielectric constant, the dimension of the ground plane may not be much larger than the dimension of the antenna. In Figure 3.20, the slot-induced maximum moves up in frequency as the ground plane width decreases.

In the E-plane oriented scaled configuration of the Chiu slots, the ground plane width was approximately $0.84\lambda_{\text{eff}}$ at 2.38 GHz. Since the ground plane width is not close to a half wavelength, the dipole excitation mode would not be excited at this frequency. However, the slots produced substantial improvement in isolation between the antennas. This points to the existence of another

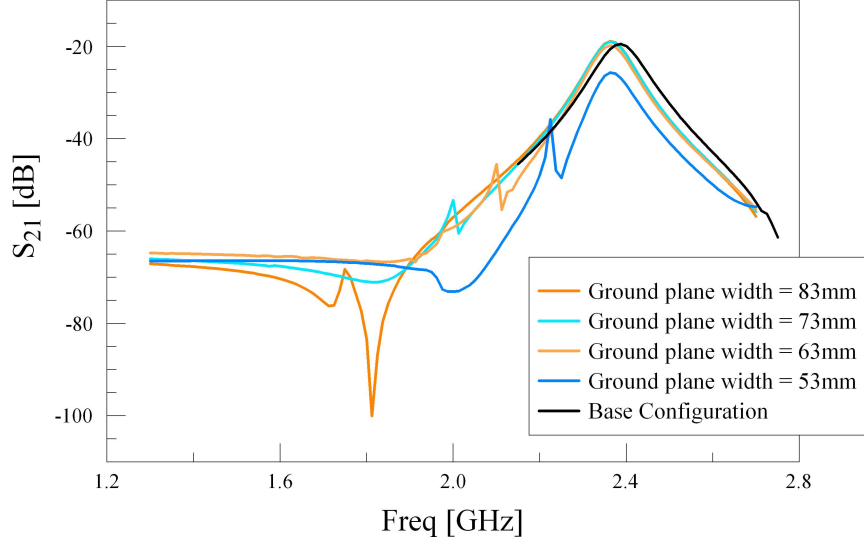


Figure 3.20: Simulated S-parameters for scaled Chiu design with varying ground plane width. Slot length = 28 mm, slot width = 1.5 mm, and slot spacing = 2 mm (results from Ansoft HFSS).

excitation mode for the Chiu slot structure. The length of an individual slot is approximately $\lambda_{\text{eff}}/4$ in the operating band. With that in mind, consider the resemblance of the strip between the slots to a CPW line. The line then transforms the apparent “open” at the ground plane edge to a “short” near the center. Munk refers to this type of behavior as a “load null” when it occurs in a frequency-selective surface [10]. The quarter-wavelength slots terminated in an open can also be considered similar to the dual of a monopole above a ground plane.

In the system that generated the data in Figure 3.6, the slots are implemented in an H-plane configuration and the ground plane size is constant at 53 mm, but some features (circled in the figure) of the frequency response shift with changing slot length. The slot length at the frequencies of the slot-induced S_{21} features is approximately $\lambda_{\text{eff}}/4$, implying that the slots are being excited independently as quarter-wavelength monopoles as they were in the E-plane configuration. The only differences between this system and the

dipole-excited system are the slot width and spacing, so it must be the choice of these dimensions that influences the characteristic impedances of the two modes and determines which mode is preferred. The peak marked with a triangle in Figure 3.6 corresponds with the dipole mode, since it is also present in Figure 3.20.

In the case of the Alvey design, our various trials of rotating and moving the slots led to two conclusions. First, the rotated blocks were less responsive to excitation than the nonrotated blocks, even when the antenna was rotated. From this it is clear that the most effective block orientation is not determined by the direction of the antenna's current, but by the distribution of the fringing fields along the nearest antenna edge. Second, since the meander-line blocks' excitation was improved when they were placed near the edge of the ground plane in the H-plane configuration but at the center in the E-plane configuration, blocks should be placed in areas where the electric fringing field from the patch edge is strongest.

3.4 Modified Designs

This investigation was undertaken because the ground plane slot designs under consideration demonstrated qualitatively different behavior when the antennas' orientation was changed or when the slots were implemented in a different system. In two of those cases, once the design was changed the slots no longer provided an in-band isolation improvement. Those were the scaled implementation of the Chiu design in the H-plane configuration (S-parameters shown in Figure 3.5) and the H-plane implementation of the Alvey design (S-parameters in Figure 3.10). In this section, we revisit those cases and introduce modifications so that the slots effectively operate to decrease coupling

in their new environment.

The Chiu slot design has a simple geometry which supports clearly identifiable modes. Here, the key information is that for excitation in the H-plane orientation, the ground plane width must be close to an effective half wavelength in the slots' composite substrate-air medium. Decreasing the ground plane width to 53 mm, barely larger than the antennas themselves, moves the slot-induced peak up in frequency but does not place it in the operating band (see Figure 3.20). It is close enough, however, that the adjacent dip reduces S_{21} by 7.4 dB. Since there are two modes present, we can also influence the slot-induced feature's location by changing the slot length. Figure 3.21 shows the S-parameters of the system when the ground plane width is 53 mm and the slot length is reduced from 28 mm to 25 mm. The slot-induced features shift further upward in frequency. Isolation shows little improvement in this configuration, increasing by 0.2 dB to 7.6 dB.

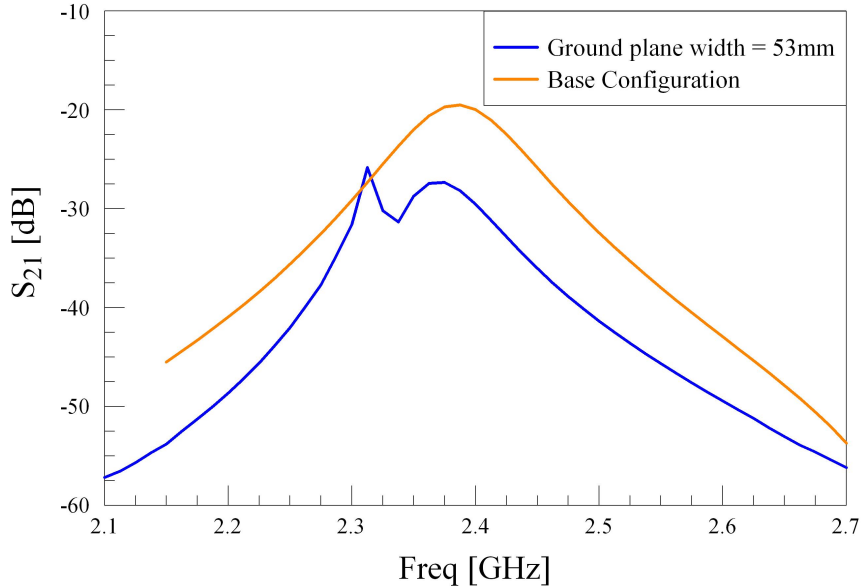


Figure 3.21: S-parameters for Chiu design operating in dipole mode with ground plane width = 53 mm, slot width = 1.5 mm, slot spacing = 2 mm, and slot length = 25 mm (results from Ansoft HFSS).

Since Alvey’s meander-line blocks performed better in the H-plane configuration when placed near the ground plane edge, similar reasoning suggested that a half-wavelength ground plane should provide better excitation of the slot structure. The Alvey design originally had a ground plane width of 83 mm. When the antennas are rotated into the H-plane configuration and the meander line blocks moved to the ground plane edges, a ground plane width of 48 mm provided best isolation between the antennas. This is $0.49\lambda_{\text{eff}}$, slightly smaller than the ground plane width for the Chiu design at this frequency. The difference may be due to additional surface inductance presented by the meander lines in the slot area, which extends the slot structure’s electrical length slightly. Figure 3.22 shows how isolation responds to changing the ground plane width. The slots induce a dip in S_{21} that moves up in frequency as the ground plane width decreases.

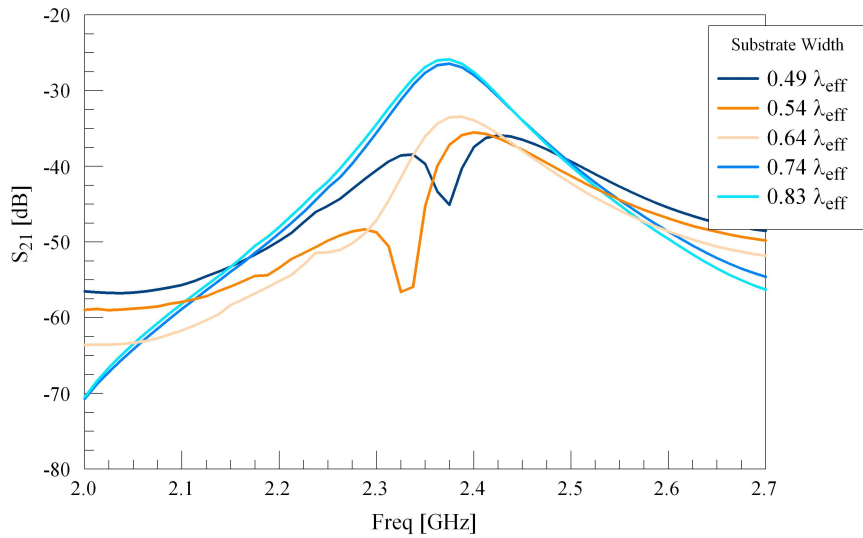


Figure 3.22: S-parameters for H-plane configuration Alvey design with center gap and varying ground plane width (results from Ansoft HFSS).

3.5 Conclusions

We have presented an analysis of how ground plane slot structures' excitation depends on both antenna orientation and slot placement. Results showed that slots must be placed near maxima of the fringing fields. This led to the conclusion that for an E-plane configuration slots should be near the center of the ground plane, while for an H-plane configuration they should be near the edges of the ground plane and the total structure's electrical length should be an effective half wavelength.

This constraint on the total structure's size also places a constraint on the size of the ground plane. If one chooses a low-dielectric substrate, the ground plane width could be very close to the antenna size, leading to strong effects from the finite ground plane. However, the modified Chiu and Alvey slot designs' final ground plane widths were slightly different. The presence of the Alvey design's meander-line blocks appears to have added a surface reactance that changed the resonant length of the slot structure. This type of effect could help mitigate the ground plane size constraint in H-plane configurations, in the same way that loading a dipole antenna can aid in miniaturization, but only within a range of ground plane widths close to an effective half wavelength.

CHAPTER 4

A CIRCUIT MODEL FOR ANTENNA SYSTEMS WITH GROUND PLANE SLOTS

This chapter presents a circuit model to represent a system with two microstrip patch antennas and a ground plane slot structure. The first section will develop a transmission line model that describes coupling between two microstrip patch antennas and the resonant slot structure. Simplifications that are possible depending on the physical configuration will also be discussed. The circuit model depends on a calculation of the mutual admittance between the antennas' radiating edges and the resonant slots in the ground plane. Because the distances involved are not large enough to permit the far field approximation, the mutual admittances must be calculated numerically. This method is briefly discussed. Finally, the model and mutual admittance calculation are employed to predict the behavior of an example design.

4.1 Transmission-Line Model

Consider two rectangular patch antennas sharing a ground plane in which a resonant slot structure is present (Figure 4.1). For the moment, it is not necessary to know their relative positions or orientations. That said, cross-polarized slots will not couple to one another, so it should be pointed out that some configurations are not relevant to the current discussion. For purposes of calculating mutual admittance, the slots and the radiating edges of each antenna will be represented by equivalent distributions of magnetic current.

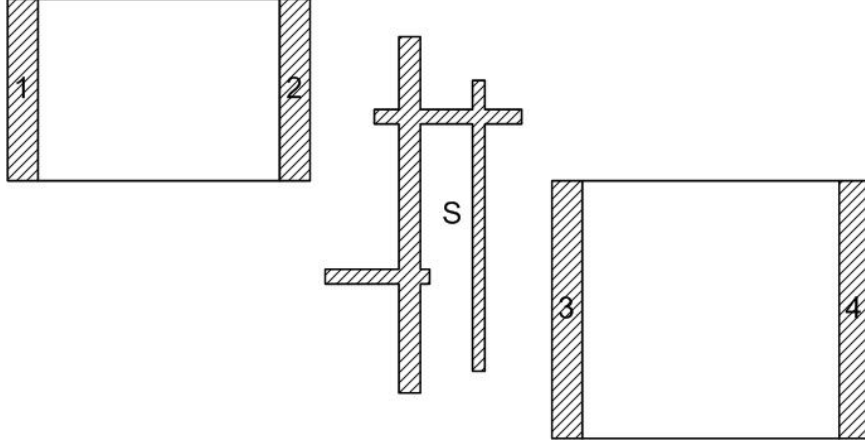


Figure 4.1: Problem geometry: two microstrip patch antennas with a shared ground plane which contains some slot structure. Electric fringing field along patches' edges is modeled as electric field in slots (areas with diagonal lines) for the purpose of self and mutual admittance calculations.

The circuit model we present in Figure 4.2 is based on the transmission line model for microstrip patch antennas [12], [13], with the addition of dependent current sources to account for mutual coupling. The presence of the sources has the same effect as a lumped mutual admittance, so we represent the coupling as a dependent source in order to obtain a more straightforward diagram. At each end of the transmission line representing each patch antenna, a shunt admittance accounts for the radiated wave (this is the self-admittance of the equivalent radiating slot [13]). Then four current sources account for coupling of that slot with the other edge of the same antenna, the two equivalent slots of the second antenna, and the ground plane slot structure. The ground plane slots are modeled simply as their own self-admittance in parallel with four current sources representing their coupling with the two equivalent slots on each of the two antennas. As shown in Figure 4.3, if the voltages at either end of a patch antenna are both defined from the patch (positive) to the ground plane (negative), then the directions of voltage definition in the equivalent radiating slots on either end must oppose each other. Although the voltages will be 180°

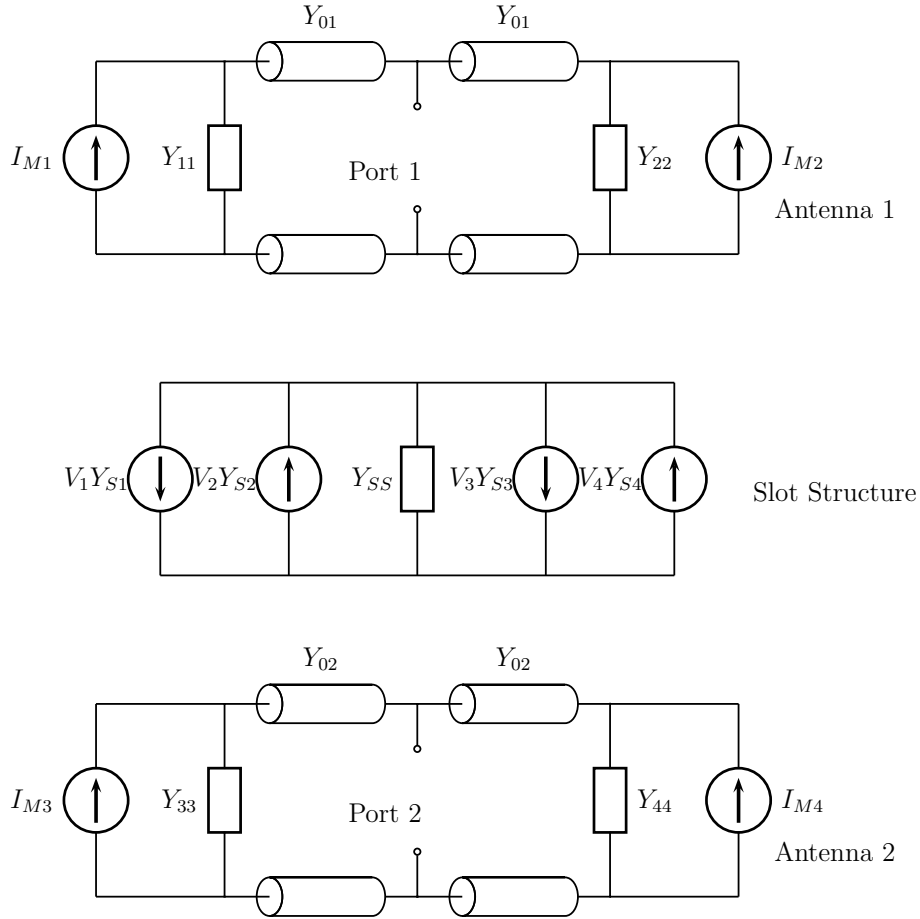


Figure 4.2: Transmission line model of two-antenna system including coupling from ground plane slot structure.

out of phase when the antenna is fed due to the length of the patch, here we are concerned with the direction of voltage definition, not the sign of the voltage itself. The orientation of the current sources in the transmission line model from [13] account for this voltage convention already. In this situation, since it is impossible for all the slot voltages to oppose all the other slot voltages, certain admittance terms undergo a sign change, as is evident in Equations (4.1) through (4.4):

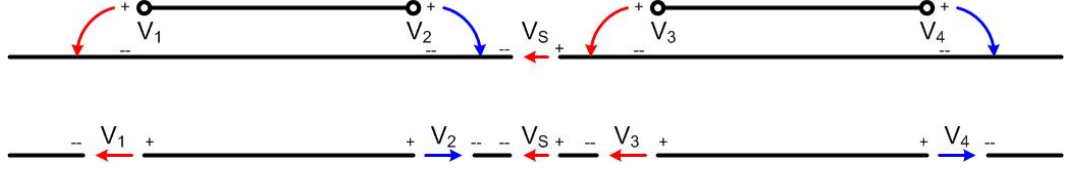


Figure 4.3: Definition of voltage for mutual admittance calculation to agree with circuit model.

$$I_{M1} = Y_{12}V_2 - Y_{13}V_3 + Y_{14}V_4 - Y_{1S}V_S \quad (4.1)$$

$$I_{M2} = Y_{21}V_1 + Y_{23}V_3 - Y_{24}V_4 + Y_{2S}V_S \quad (4.2)$$

$$I_{M3} = -Y_{31}V_1 + Y_{23}V_2 + Y_{34}V_4 - Y_{3S}V_S \quad (4.3)$$

$$I_{M4} = Y_{41}V_1 - Y_{42}V_2 + Y_{43}V_3 + Y_{4S}V_S \quad (4.4)$$

In certain system configurations, the model can be simplified. For instance, if the antennas are arranged along a line in their E-planes, as in Figure 4.4, coupling from the effective slots at the far edges of each antenna will be weaker than the contribution from the edges closer to the center, especially if the edge-to-edge separation is not large. Therefore, depending on the degree of precision desired and the separation between the antennas, current sources that represent coupling involving these edges may be neglected. The obvious choice is to eliminate the terms that couple the far edges to one another, but if the edge-to-edge antenna spacing is less than the length of the patch, it may also be reasonable to neglect the far edge slots' coupling with the center edge slots and the ground plane slots. That leaves us to model the interaction of only three structures, rather than five (Figure 4.5).

If the antennas are aligned along a line through their H-planes and closely spaced, the nonradiating edges' fringing fields may also contribute to coupling. These can be included in the model by modifying the radiating edge equivalent slots into a U-shape whose arms each include half of one nonradiating slot's

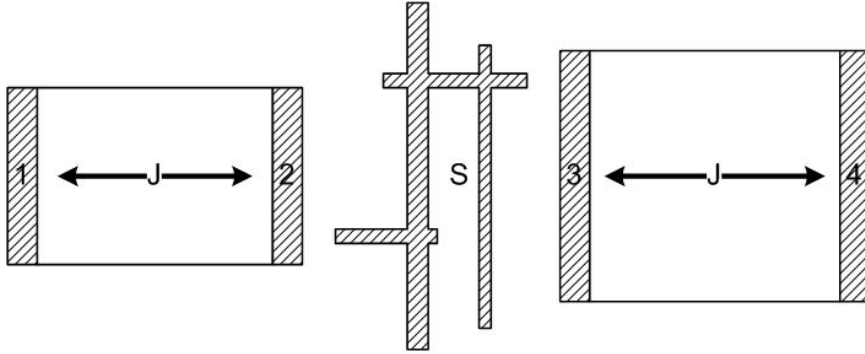


Figure 4.4: Antennas closely spaced and arranged in a line along their E-planes, which can be approximated with a simpler circuit model.

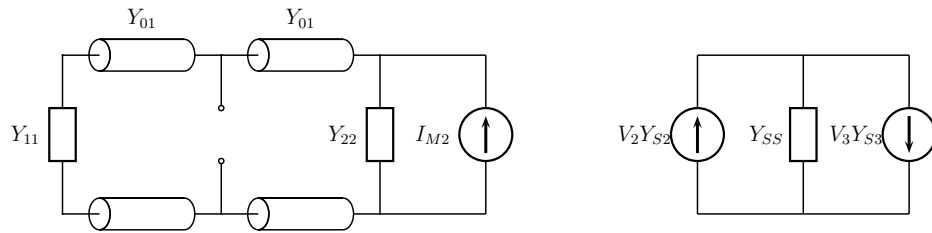


Figure 4.5: Simplified transmission line model for closely spaced E-plane oriented configuration. Antenna 2, not pictured, is a mirror image of Antenna 1 (with appropriate substitution of component values).

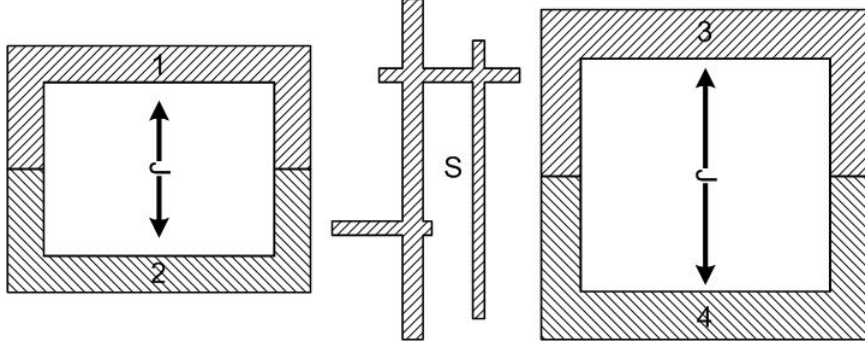


Figure 4.6: H-plane configuration geometry with radiating edge effective slots modified into U shape that includes nonradiating edges' field distribution.

sinusoidal field distribution (Figure 4.6). Those slots are then included in the circuit model as before. If the antenna spacing is very small, this will not appropriately model the coupling between the antennas, because the contribution of the nonradiating edges to coupling would be greater. The effect of this would be a per-unit-length mutual admittance, at which point the antennas may be better treated as a pair of coupled lines. In situations where the antenna spacing is small enough that one wishes to include the nonradiating slots but large enough that a coupled-line model is inappropriate, conversion to U-shaped slots can account for the mutual coupling due to the nonradiating edges. The approach preserves the model's simplicity at the cost of changing a per-unit-length mutual admittance to a lumped mutual admittance that terminates the transmission line model.

To obtain a solution for the current and voltage at Port 1 and at Port 2, we begin by defining ports for the ground plane slots and each of the antennas' equivalent radiating slots, as shown in Figure 4.7. The slot ports' voltages and currents are related by a set of mutual admittances, as in Equation (4.5).

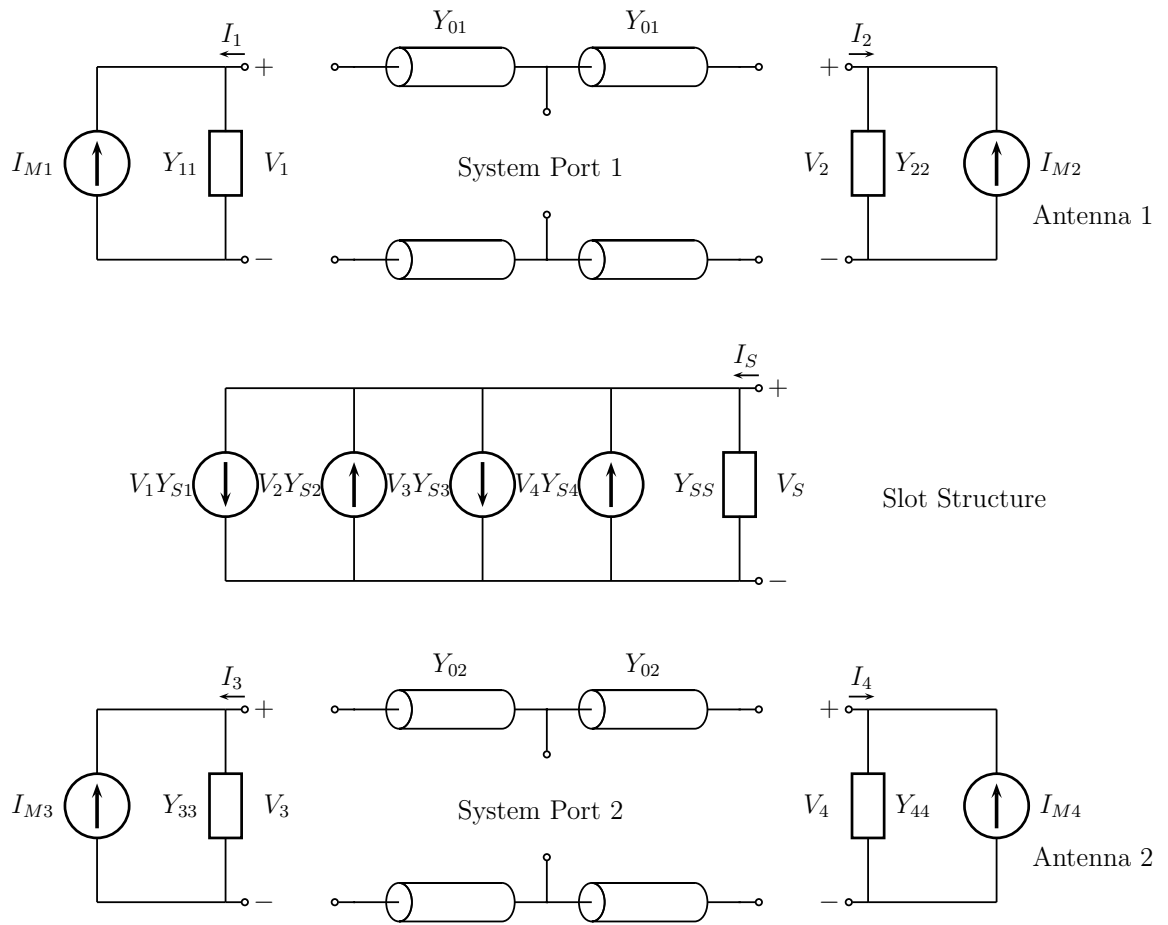


Figure 4.7: Transmission line model of two-antenna system including coupling from ground plane slot structure and slot port definitions for circuit analysis.

$$\begin{bmatrix} I_1 \\ I_2 \\ I_3 \\ I_4 \\ 0 \end{bmatrix} = \begin{bmatrix} Y_{11} & Y_{12} & -Y_{13} & Y_{14} & -Y_{1S} \\ Y_{21} & Y_{22} & Y_{23} & -Y_{24} & Y_{2S} \\ -Y_{31} & Y_{32} & Y_{33} & Y_{34} & -Y_{3S} \\ Y_{41} & -Y_{42} & Y_{43} & Y_{44} & Y_{4S} \\ -Y_{S1} & Y_{S2} & -Y_{S3} & Y_{S4} & Y_{SS} \end{bmatrix} \begin{bmatrix} V_1 \\ V_2 \\ V_3 \\ V_4 \\ V_S \end{bmatrix} \quad (4.5)$$

V_S is not directly connected to any port, so it is a known function of the other four voltages:

$$V_S = \frac{1}{Y_{SS}}(-Y_{S1}V_1 + Y_{S2}V_2 - Y_{S3}V_3 + Y_{S4}V_4) \quad (4.6)$$

We can substitute this expression into Equation (4.5) to obtain

$$\begin{bmatrix} I_1 \\ I_2 \\ I_3 \\ I_4 \\ 0 \end{bmatrix} = \begin{bmatrix} & & & & \\ & & & & \\ & & & & \\ & & & & \\ & & & & \end{bmatrix} \begin{bmatrix} Y_c & & & & \\ & & & & \\ & & & & \\ & & & & \\ & & & & \end{bmatrix} \begin{bmatrix} V_1 \\ V_2 \\ V_3 \\ V_4 \\ 0 \end{bmatrix} \quad (4.7)$$

where the matrix Y_c is the admittance matrix in Equation (4.5) and the matrix A is given by

$$\begin{bmatrix} A \end{bmatrix} = \begin{bmatrix} 1 & 0 & 0 & 0 & 0 \\ 0 & 1 & 0 & 0 & 0 \\ 0 & 0 & 1 & 0 & 0 \\ 0 & 0 & 0 & 1 & 0 \\ -Y_{S1}/Y_{SS} & Y_{S2}/Y_{SS} & -Y_{S3}/Y_{SS} & Y_{S4}/Y_{SS} & 0 \end{bmatrix} \quad (4.8)$$

We also know that Slot 1 and Slot 2 are connected in parallel by

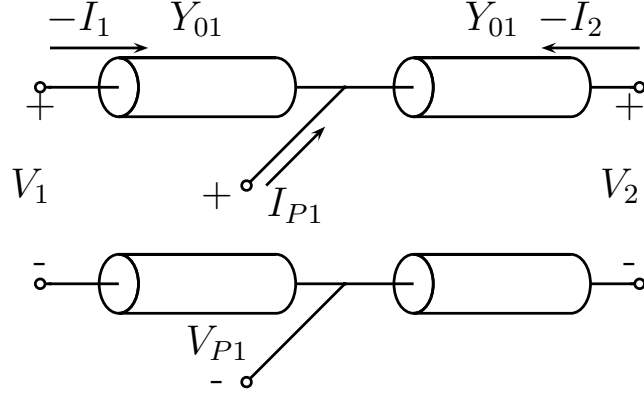


Figure 4.8: Diagram of the connection between Port 1, Slot 1, and Slot 2, including voltage and current definitions.

transmission lines to Port 1, as shown in Figure 4.8. Slot 3 and Slot 4 are similarly connected to Port 2. We can now create admittance matrices for the relationships between these voltages and currents:

$$\begin{bmatrix} I_{P1} \\ -I_1 \\ -I_2 \end{bmatrix} = \begin{bmatrix} jY_{01}(\cot(\beta_1 L_{L1}) + \cot(\beta_1 L_{R1})) & -jY_{01}/\sin(\beta_1 L_{L1}) & -jY_{01}/\sin(\beta_1 L_{R1}) \\ -jY_{01}/\sin(\beta_1 L_{L1}) & jY_{01} \cot(\beta_1 L_{L1}) & 0 \\ -jY_{01}/\sin(\beta_1 L_{R1}) & 0 & jY_{01} \cot(\beta_1 L_{R1}) \end{bmatrix} \times \begin{bmatrix} V_{P1} \\ V_1 \\ V_2 \end{bmatrix} \quad (4.9)$$

$$\begin{bmatrix} I_{P2} \\ -I_3 \\ -I_4 \end{bmatrix} = \begin{bmatrix} jY_{02}(\cot(\beta_2 L_{L2}) + \cot(\beta_2 L_{R2})) & -jY_{02}/\sin(\beta_2 L_{L2}) & -jY_{02}/\sin(\beta_2 L_{R2}) \\ -jY_{02}/\sin(\beta_2 L_{L2}) & jY_{02} \cot(\beta_2 L_{L2}) & 0 \\ -jY_{02}/\sin(\beta_2 L_{R2}) & 0 & jY_{02} \cot(\beta_2 L_{R2}) \end{bmatrix} \times \begin{bmatrix} V_{P2} \\ V_3 \\ V_4 \end{bmatrix} \quad (4.10)$$

The inverses of the above Y matrices give us V_{P1} , V_{P2} , V_1 , V_2 , V_3 , and V_4 in terms of I_{P1} , I_{P2} , I_1 , I_2 , I_3 , and I_4 . Substituting those relationships back into Equation (4.7), we obtain

$$\begin{bmatrix} I_1 \\ I_2 \\ I_3 \\ I_4 \\ 0 \end{bmatrix} = \begin{bmatrix} & Y_c & & & \\ & & & & \\ & & & & \\ & & & & \\ & & & & \end{bmatrix} \begin{bmatrix} A & & & & \\ & & & & \\ & & & & \\ & & & & \\ & & & & \end{bmatrix} \begin{bmatrix} Z_{1P1}I_{P1} - Z_{11}I_1 - Z_{12}I_2 \\ Z_{2P1}I_{P1} - Z_{21}I_1 - Z_{22}I_2 \\ Z_{3P2}I_{P2} - Z_{33}I_3 - Z_{34}I_4 \\ Z_{4P2}I_{P2} - Z_{43}I_3 - Z_{44}I_4 \\ 0 \end{bmatrix} \quad (4.11)$$

From 4.11, a little rearranging obtains

$$\begin{aligned}
 & \left[\begin{array}{c} \left[\text{Identity} \right] + \left[\begin{array}{c} Y_c \end{array} \right] \left[\begin{array}{c} A \end{array} \right] \left[\begin{array}{c} Z_{11} \quad Z_{12} \quad 0 \quad 0 \quad 0 \\ Z_{21} \quad Z_{22} \quad 0 \quad 0 \quad 0 \\ 0 \quad 0 \quad Z_{33} \quad Z_{34} \quad 0 \\ 0 \quad 0 \quad Z_{43} \quad Z_{44} \quad 0 \\ 0 \quad 0 \quad 0 \quad 0 \quad 0 \end{array} \right] \left[\begin{array}{c} I_1 \\ I_2 \\ I_3 \\ I_4 \\ 0 \end{array} \right] \\
 & = \left[\begin{array}{c} Y_c \end{array} \right] \left[\begin{array}{c} A \end{array} \right] \left[\begin{array}{c} Z_{1P1}I_{P1} \\ Z_{2P1}I_{P1} \\ Z_{3P2}I_{P2} \\ Z_{4P2}I_{P2} \\ 0 \end{array} \right] \quad (4.12)
 \end{aligned}$$

In Equation (4.12) we have the currents I_1 , I_2 , I_3 , and I_4 in terms of I_{P1} and I_{P2} . To obtain the voltages V_{P1} and V_{P2} we refer back to Equations (4.9) (4.10); the inverses of the admittance matrices used in those equations give us V_{P1} and V_{P2} in terms of the currents obtained in Equation (4.12).

In the case of the simplified E-plane configuration model, the calculation is greatly simplified because coupling is restricted to a 2-port network involving Slot 2, the ground plane slot structure, and Slot 3, as shown in Figure 4.9. This network can be described by an $ABCD$ matrix. The transmission lines connecting this network to the antenna ports can also be represented as $ABCD$ matrices and included in a cascade. We are left with one large network represented by the cascade of $ABCD$ matrices, on which the left-hand port is connected in parallel to Port 1 and the left half of Antenna 1, and the right-hand port is connected in parallel to Port 2 and the right half of Antenna 2.

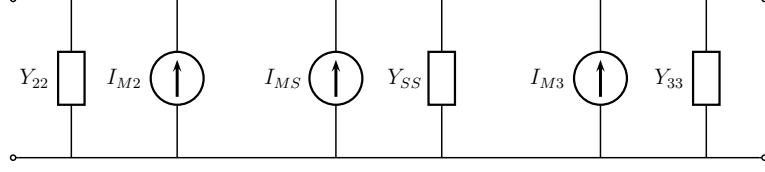


Figure 4.9: Two-port network including all mutual coupling in the simplified E-plane model.

The central network including the slots' mutual coupling is described by

$$A_c = \frac{Y_{33} - Y_{S3}Y_{3S}/Y_{SS}}{Y_{32} + Y_{S2}Y_{3S}/Y_{SS}} \quad (4.13)$$

$$B_c = \frac{1}{Y_{32} + Y_{S2}Y_{3S}/Y_{SS}} \quad (4.14)$$

$$C_c = \left(Y_{22} - \frac{Y_{S2}Y_{2S}}{Y_{SS}} \right) \left(\frac{Y_{33} - Y_{S3}Y_{3S}/Y_{SS}}{Y_{32} + Y_{S2}Y_{3S}/Y_{SS}} \right) - \left(Y_{23} + \frac{Y_{2S}Y_{S3}}{Y_{SS}} \right) \quad (4.15)$$

$$D_c = \frac{Y_{22} - Y_{2S}Y_{S2}/Y_{SS}}{Y_{32} + Y_{S2}Y_{3S}/Y_{SS}} \quad (4.16)$$

Then we can create $ABCD_{\text{mid}}$, which describes everything between Port 1 and Port 2 in Figure 4.5.

$$\begin{bmatrix} A_{\text{mid}} & B_{\text{mid}} \\ C_{\text{mid}} & D_{\text{mid}} \end{bmatrix} = \begin{bmatrix} \cos(\beta_1 L_{R1}) & jZ_{01} \sin(\beta_1 L_{R1}) \\ jY_{01} \sin(\beta_1 L_{R1}) & \cos(\beta_1 L_{R1}) \end{bmatrix} \times \begin{bmatrix} A_c & B_c \\ C_c & D_c \end{bmatrix} \times \begin{bmatrix} \cos(\beta_2 L_{L2}) & jZ_{02} \sin(\beta_2 L_{L2}) \\ jY_{02} \sin(\beta_2 L_{L2}) & \cos(\beta_2 L_{L2}) \end{bmatrix} \quad (4.17)$$

$$A_{\text{mid}} = \cos(\beta_1 L_{R1}) (A_c \cos(\beta_2 L_{L2}) + jB_c Y_{02} \sin(\beta_2 L_{L2})) \quad (4.18)$$

$$+ jZ_{01} \sin(\beta_1 L_{R1}) (C_c \cos(\beta_2 L_{L2}) + jD_c Y_{02} \sin(\beta_2 L_{L2})) \quad (4.19)$$

$$B_{\text{mid}} = \cos(\beta_1 L_{R1}) (jZ_{02}A_c \sin(\beta_2 L_{L2}) + B_c \cos(\beta_2 L_{L2})) \quad (4.20)$$

$$+ jZ_{01} \sin(\beta_1 L_{R1}) (jZ_{02}C_c \sin(\beta_2 L_{L2}) + D_c \cos(\beta_2 L_{L2})) \quad (4.21)$$

$$C_{\text{mid}} = jY_{01} \sin(\beta_1 L_{R1}) (A_c \cos(\beta_2 L_{L2}) + jB_c Y_{02} \sin(\beta_2 L_{L2})) \quad (4.22)$$

$$+ \cos(\beta_1 L_{R1}) (C_c \cos(\beta_2 L_{L2}) + jD_c Y_{02} \sin(\beta_2 L_{L2})) \quad (4.23)$$

$$D_{\text{mid}} = jY_{01} \sin(\beta_1 L_{R1}) (jZ_{02}A_c \sin(\beta_2 L_{L2}) + B_c \cos(\beta_2 L_{L2})) \quad (4.24)$$

$$+ \cos(\beta_1 L_{R1}) (jZ_{02}C_c \sin(\beta_2 L_{L2}) + D_c \cos(\beta_2 L_{L2})) \quad (4.25)$$

Finally, we can use this network representation and the input impedances of the left half of Antenna 1 (Z_{t1}) and the right half of Antenna 2 (Z_{t4}) to find $ABCD_t$ for the total network connected to Ports 1 and 2 in the simplified E-plane model.

$$Z_{t1} = Z_{01} \frac{1/Y_{11} + jZ_{01} \tan(\beta_1 L_{L1})}{Z_{01} + j(1/Y_{11}) \tan(\beta_1 L_{L1})} \quad (4.26)$$

$$Z_{t4} = Z_{02} \frac{1/Y_{44} + jZ_{02} \tan(\beta_2 L_{R2})}{Z_{02} + j(1/Y_{44}) \tan(\beta_2 L_{R2})} \quad (4.27)$$

$$A_t = A_{\text{mid}} \quad (4.28)$$

$$B_t = B_{\text{mid}} \quad (4.29)$$

$$C_t = \frac{A_{\text{mid}}(C_{\text{mid}}Z_{t4} + D_{\text{mid}})}{A_{\text{mid}}Z_{t4}B_{\text{mid}}} \quad (4.30)$$

$$D_t = D_{\text{mid}} + \frac{B_{\text{mid}}}{Z_{t1}} \quad (4.31)$$

4.2 Self and Mutual Admittance Calculation

Mutual coupling between the slots in this model has been calculated using the induced EMF method, as described in [14] and implemented in [13]. We treat the problem by considering one pair of slots at a time and finding their mutual admittance. In general, the mutual admittance between two slots is given by

$$Y_{21}^* = \frac{-1}{V_1^* V_2} \iint \vec{H}_1^* \cdot \vec{M}_2 dS_2 \quad (4.32)$$

Above, \vec{H}_1 is the field due to the impressed magnetic current in Slot 1 when Slot 2 is not present, \vec{M}_2 is the impressed magnetic current in Slot 2, and the integral is taken over the area of Slot 2. V_1 and V_2 are voltages defined across the slots. One can choose any path across a slot to define voltage, so that field and voltage are related by integration along that path. The expressions for the field and magnetic current will carry a factor of V_n which will simply be canceled by the leading $1/V_n$ factor.

First the magnetic field due to Slot 1 in the absence of Slot 2 must be calculated. We use the equivalence principle to replace the field in the slot, \vec{E}_1 , by a magnetic surface current $\vec{M}_1 = -\hat{z} \times \vec{E}_1$, then to remove the ground plane by doubling \vec{M}_1 [15]. The field we calculate from this new problem geometry will be valid in the upper half space of the original problem (with the ground plane present).

The mutual admittance can be obtained using a 3×3 matrix \tilde{H} representing the magnetic field components of an arbitrarily directed infinitesimal magnetic dipole, as in Equation (4.33) [13].

$$Y_{21}^* = \frac{-1}{V_1^* V_2} \iint \iint \vec{M}_1^*(r_1) \cdot \tilde{H}^*(r_2, r_1) \cdot \vec{M}_2(r_2) dS_1 dS_2 \quad (4.33)$$

Because both \vec{M}_1 and \vec{M}_2 are, except in special cases, purely \hat{y} directed currents, we are mainly concerned with the \hat{y} component of the magnetic field that would be radiated by a \hat{y} directed magnetic dipole, the H_{yy} component of \tilde{H} .

$H_{yy}(r_2, r_1)$ is given by

$$H_{yy}(r_2, r_1) = \frac{j e^{-jk_0 r}}{2\pi k_0 \eta_0} \frac{1}{2} \left(\left(\frac{jk_0}{r^2} + \frac{1}{r^3} \right) \cos^2 \theta^{(y)} + \frac{1}{2} \left(\frac{k_0^2}{r} - \frac{jk_0}{r^2} + \frac{1}{r^3} \right) \sin^2 \theta^{(y)} \right) \quad (4.34)$$

where $\theta^{(y)}$ and $\phi^{(y)}$ are defined so that

$$\sin \theta^{(y)} = \sqrt{\Delta z^2 + \Delta x^2} / r \quad (4.35)$$

$$\sin \phi^{(y)} = \Delta x / (r \sin \theta^{(y)}) \quad (4.36)$$

$$\cos \theta^{(y)} = \Delta y / r \quad (4.37)$$

$$\cos \phi^{(y)} = \Delta y / (r \sin \theta^{(y)}) \quad (4.38)$$

Should we be interested in including fields from \hat{x} directed currents, for instance in the case of close coupling in the H-plane, we would need to include H_{xy} , H_{yx} , and H_{xx} as well. H_{xy} , the \hat{x} -directed magnetic field due to a \hat{y} -directed infinitesimal magnetic dipole, is given by

$$H_{xy}(r_2, r_1) = \frac{j e^{-jk_0 r}}{2\pi k_0 \eta_0} \frac{1}{2} \left(- \left(\frac{jk_0}{r^2} + \frac{1}{r^3} \right) \cos \theta^{(y)} \sin \theta^{(y)} \sin \phi^{(y)} + \frac{1}{2} \left(\frac{k_0^2}{r} - \frac{jk_0}{r^2} + \frac{1}{r^3} \right) \sin \theta^{(y)} \cos \theta^{(y)} \sin \phi^{(y)} \right) \quad (4.39)$$

The relevant magnetic field components due to \hat{x} -directed magnetic dipoles are

$$H_{xx}(r_2, r_1) = \frac{j e^{-jk_0 r}}{2\pi k_0 \eta_0} \frac{1}{2} \left(\left(\frac{jk_0}{r^2} + \frac{1}{r^3} \right) \cos^2 \theta^{(x)} + \frac{1}{2} \left(\frac{k_0^2}{r} - \frac{jk_0}{r^2} + \frac{1}{r^3} \right) \sin^2 \theta^{(x)} \right) \quad (4.40)$$

$$H_{yx}(r_2, r_1) = \frac{je^{-jk_0r}}{2\pi k_0 \eta_0} \frac{1}{2} \left(- \left(\frac{jk_0}{r^2} + \frac{1}{r^3} \right) \cos \theta^{(x)} \sin \theta^{(x)} \cos \phi^{(x)} + \right. \\ \left. \frac{1}{2} \left(\frac{k_0^2}{r} - \frac{jk_0}{r^2} + \frac{1}{r^3} \right) \sin \theta^{(x)} \cos \theta^{(x)} \cos \phi^{(x)} \right) \quad (4.41)$$

where $\theta^{(x)}$ and $\phi^{(x)}$ are defined as

$$\sin \theta^{(x)} = \sqrt{\Delta z^2 + \Delta y^2}/r \quad (4.42)$$

$$\sin \phi^{(x)} = \Delta z/(r \sin \theta^{(x)}) \quad (4.43)$$

$$\cos \theta^{(x)} = \Delta x/r \quad (4.44)$$

$$\cos \phi^{(x)} = \Delta y/(r \sin \theta^{(x)}) \quad (4.45)$$

The mutual admittance calculation just presented assumes impressed magnetic currents, which renders it unsuitable for calculation of self-admittance. Since the slots in the ground plane do not necessarily have a uniform field distribution, closed-form expressions for a slot's self-admittance may not be applied. Instead, we calculate self-admittance using a spectral method similar to the one described by Harrington in [16, Section 4.11], modified to account for a slot of finite extent. The tangential electric field distribution in the slot must be known or assumed.

$$G_s = \frac{1}{a^2} \int_0^k \int_0^{2\pi} \frac{j}{\sqrt{k^2 - k_x^2 - k_y^2}} \frac{k^2 - k_y^2}{j\omega\mu} \left| \tilde{E}_x(k_x, k_y) \right|^2 k_\rho dk_\rho d\alpha \quad (4.46)$$

$$B_s = \frac{1}{a^2} \int_k^\infty \int_0^{2\pi} \frac{j}{\sqrt{k^2 - k_x^2 - k_y^2}} \frac{k^2 - k_y^2}{j\omega\mu} \left| \tilde{E}_x(k_x, k_y) \right|^2 k_\rho dk_\rho d\alpha \quad (4.47)$$

Above, $k_x = k_\rho \cos \alpha$, $k_y = k_\rho \sin \alpha$, and \tilde{E}_x is the Fourier transform of the \hat{x} directed electric field component in the slot. These expressions were developed

for a slot in a ground plane surrounded by free space. For slots with a substrate, we approximate the effective medium experienced by the slot by setting $k = 2\pi/\lambda_{\text{eff}}$. This approach models the correct electrical size of the slots but does not include the effect of surface waves. Other options are to treat the slots as though they are surrounded by free space [17], or to account for surface wave effects by explicitly modeling the substrate [18].

By referring to Babinet's principle, we can perform a simple test of the self-admittance calculation by relating the self-admittance of a slot dipole to the well-known self-impedance of its dual, a metal dipole:

$$\frac{Z_{\text{metal}}}{4\eta^2} = Y_{\text{slot}} \quad (4.48)$$

The self-admittance of a 61 mm slot dipole (without a substrate) was calculated (Figure 4.10) using both Babinet's principle and the method from [16]. The self-impedance of the metal dipole was calculated from the expression given in [19] for a cylindrical dipole; discrepancy between the two results is likely due to the fact that a cylindrical dipole is not precisely the dual of a planar slot.

4.3 Results

Using the simplified E-plane model presented in Section 4.1 and the mutual admittance calculation discussed in Section 4.2, S-parameters were calculated for Chiu slot structure scaled by a factor of 0.45 and implemented on the E-plane base configuration (Figure 4.11). The calculation correctly predicts the presence of the slot-induced dip in S_{21} , but the dip occurs at 2.4875 GHz in the calculated data as compared to 2.2625 GHz in the simulated data. This constitutes a 9.9% prediction error in frequency, which may be due either to our

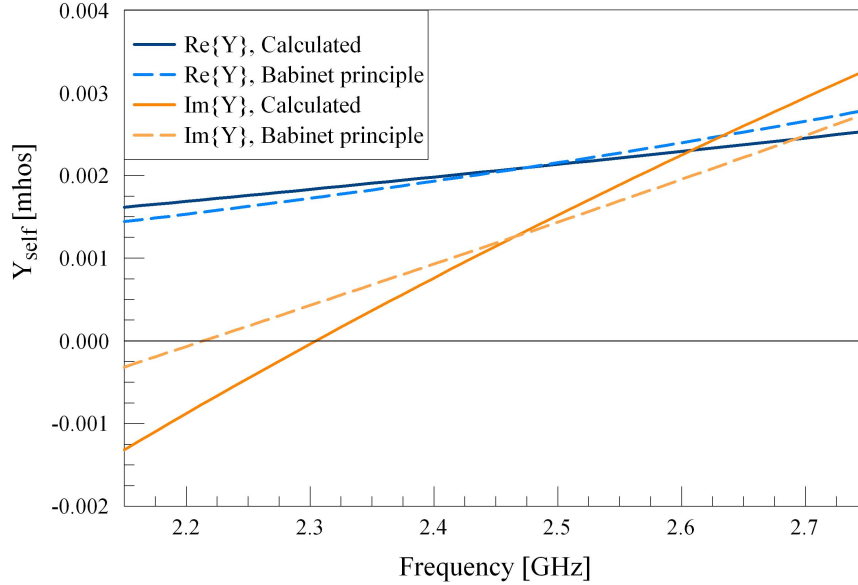


Figure 4.10: Real and imaginary parts of self-admittance of a 61 mm slot dipole as calculated from [16] (solid lines) and using Babinet’s principle with the self-impedance of a cylindrical dipole, from [19].

use of the simplified E-plane model for calculation, or to the fact that the admittance calculations represented the substrate as a uniform effective dielectric constant rather than accounting for it precisely. More accurate results may be obtainable by employing the method described in [18] for calculating the fields from a slot with a substrate. The calculation also generally overestimates coupling compared to the simulated data.

4.4 Analysis

The circuit equations in Section 4.1 are too convoluted to yield much insight into the system’s operation by direct examination. However, in conjunction with the circuit model’s geometry they can help us arrive at design guidelines.

Consider a single patch antenna in the absence of the slots and coupling antenna, whose transmission line model is shown in Figure 4.12. The model

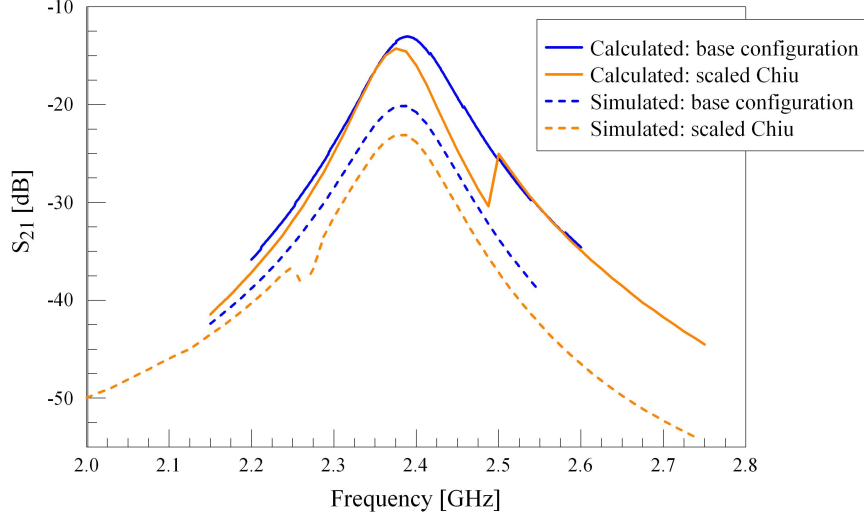


Figure 4.11: Calculated S-parameters for scaled Chiu slot structure implemented on E-plane oriented base configuration, compared to calculated base configuration S-parameters and simulated results for the same models.

includes coupling between the two radiating edges of the antenna. If a second antenna and ground plane slots are added, the effect on this antenna is the addition of three more dependent current sources on each end of the model, as in Figure 4.13. The point of including the ground plane slot structure is to remove the effect of the first antenna on the second antenna (and vice versa). If Antenna 1 is active, this means that we would like to have $I_{M3} = 0$ and $I_{M4} = 0$, so that Antenna 1 produces no effect on Antenna 2.

I_{M3} and I_{M4} are given by

$$I_{M3} = -Y_{31}V_1 + Y_{23}V_2 + Y_{34}V_4 - Y_{3S}V_S \quad (4.49)$$

$$I_{M4} = Y_{41}V_1 - Y_{42}V_2 + Y_{43}V_3 + Y_{4S}V_S \quad (4.50)$$

In order to arrive at a more conceptual understanding of the situation, we will address the simplified E-plane model for closely spaced antennas. In that

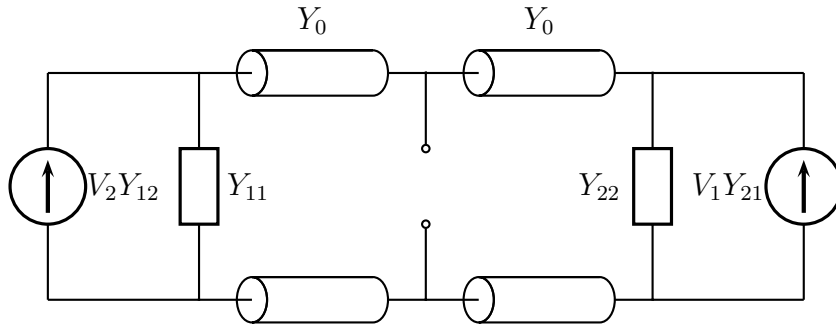


Figure 4.12: Transmission line model for single patch antenna, including coupling between edge slots.

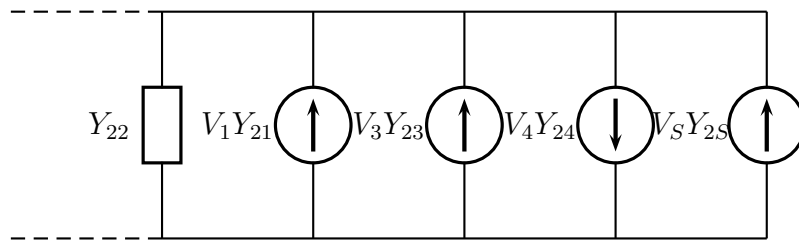


Figure 4.13: Dependent current sources on one radiating edge of one patch in the presence of ground plane slots and a second antenna.

case, we neglect coupling with Slot 4, and I_{M4} goes to zero. We are left with

$$I_{M3} = V_2 Y_{32} - V_S Y_{3S} \quad (4.51)$$

$$= V_2 Y_{32} - \frac{Y_{3S}}{Y_{SS}} (Y_{S2} V_2 - Y_{S3} V_3) \quad (4.52)$$

$$= V_2 Y_{32} - \frac{Y_{3S}}{Y_{SS}} \left(Y_{S2} V_2 - \frac{Y_{S3}}{Y_{33}} I_{M3} \right) \quad (4.53)$$

$$I_{M3} = V_2 \frac{Y_{32} - \frac{Y_{3S} Y_{S2}}{Y_{SS}}}{1 - \frac{Y_{3S} Y_{S3}}{Y_{SS} Y_{33}}} \quad (4.54)$$

In order to remove the excitation of the second antenna, the two terms in the denominator of I_{M3} must cancel, resulting in Equation (4.55). The sign of the second term in Equation (4.55) is negative for this case, but for other slot pairs it depends on the direction of voltage definition across the two equivalent radiating slots, which is a consequence of the choice of slots and the orientation of the antennas with respect to one another.

$$Y_{32} - \frac{Y_{3S} Y_{S2}}{Y_{SS}} = 0 \quad (4.55)$$

Since we expect that Y_{S2} and Y_{3S} are not large, Y_{SS} should be very small in order to present an adequate susceptance. This suggests that the ground plane slots' behavior should resemble a parallel-resonant "tank circuit," since that is an effective way to present a very small admittance. The implication of Equation (4.55) is that the ground plane slot structure should resonate as part of a larger circuit that includes the mutual admittances between itself and the antennas' radiating edge slots.

4.5 Conclusions

In this chapter we have presented a circuit model that accounts for the mutual admittance among radiating edge slots on two patch antennas and a ground plane slot structure. We have analyzed the circuit model and presented expressions from which $ABCD$ parameters can be derived. In addition, a simplified circuit model was presented for one system configuration, which aided in the conceptual analysis of the circuit model's implications. Finally, this conceptual analysis led to an approximate condition that yields some design guidelines for ground plane slot structures in general.

CHAPTER 5

A NOVEL GROUND PLANE SLOT DESIGN

Of the two ground plane slot structure designs that have been investigated here, both have disadvantages that make their implementation in new systems difficult. The Alvey design is complicated and presents an unknown surface reactance that changes the effective wavelength in the slot medium, forcing the engineer to use an iterative design process. It is difficult to predict the cumulative effect of local inductances and capacitances on the overall admittance behavior of the meander-line blocks. The Chiu design is simpler but requires its slots to be terminated with the edge of the ground plane, constraining the ground plane width in some situations and making it unsuitable for planar arrays. In this chapter we design a new ground plane slot structure using the information and concepts developed in previous chapters. The slot structure will have a simple, explicit design and will not place any requirements on the ground plane width.

5.1 Mustache Design Concept

From Chapter 4, we know that the slot structure must be a resonator which couples well to the antennas' radiating edge slots. The ground plane slots' self-admittance and their mutual admittances with nearby antennas should be specific to the system configuration, so at this point our task is merely to choose a resonator for which those values can be easily tuned.

The simplest and most well-understood slot structure we can choose is a straight one, like that of the Chiu design. In order to remove the requirement that the slot be terminated at the ground plane, we examine the relationship of current and voltage at some location l_1 on a shorted slot:

$$\frac{V}{I} = Z_{\text{in}1} = jZ_{01} \tan(\beta l_1) \quad (5.1)$$

If both ends are shorted, a resonant slot has $L = n\lambda_s/2$ at its operating frequency. We can also write the input impedance looking in the other direction at l_1 :

$$Z_{\text{in}2} = jZ_{01} \tan(\beta(L - l_1)) \quad (5.2)$$

$$= jZ_{01} \tan\left(\frac{2\pi}{\lambda_s}(n\lambda_s/2 - l_1)\right) \quad (5.3)$$

$$= -jZ_{01} \tan(\beta l_1) \quad (5.4)$$

$$= Z_{\text{in}1}^* \quad (5.5)$$

If we terminate the slot with an input impedance equal to $Z_{\text{in}2}$ from Equation (5.4), we can create a resonant slot of any length because, as far as the voltage and current are concerned, it will still appear to be terminated by a short at L .

The termination impedance will be provided by one or more shorted stub slots. If it is necessary to use miniaturizing techniques like spiraling or meandering, it is best to choose these slots to be very narrow so that the miniaturization technique has minimal effect on the reactance they present. The input reactance of a shorted stub is given by

$$jX_{\text{in}S} = jZ_{02} \tan(\beta l_2) \quad (5.6)$$

For this work we will use two stubs to provide the termination impedance. In order to preserve the current distribution of a resonant half-wavelength slot, the relationship between Z_{in1} and X_{inS} when there are two stubs of the same length is

$$Z_{in2} = -Z_{in1} = 2jX_{inS} \quad (5.7)$$

With the stubs in place, the slot design resembles a mustache, so this will be referred to as the mustache design. We can now design a resonant slot of arbitrary length to fit almost any ground plane and antenna spacing requirements. In the next section, we will design a slot structure for the H-plane base configuration from Chapter 3.

5.2 Sample Design for H-Plane Configuration

The ground plane width of the H-plane base configuration is 83 mm. We would like to choose an arbitrary slot structure length that will fit in the system without requiring any changes to the dimensions of the ground plane, so let the total length of the slot structure be 65 mm, ending 9 mm from each edge of the ground plane.

We arbitrarily choose the main slot width to be 2 mm. The stub width is chosen to be 0.3 mm, the narrowest slot that can be fabricated on the Electromagnetics Laboratory's milling machine. Characteristic impedance and effective wavelength values for these slotline widths, calculated from the expressions in [20], are given in Table 5.1.

We have quite a lot of freedom to choose the lengths of the individual resonators, as long as they fit within the space allotted for the entire structure. The slot structure has a total length of 65 mm, leaving a 2 mm gap between the ends of the mustache slots (each mustache slot has length 31.5 mm). The lines

Table 5.1: Table of slot characteristic impedance and effective wavelength values, calculated from [20].

	$W = 2 \text{ mm}$		$W = 0.3 \text{ mm}$	
	$Z_0 \text{ } (\Omega)$	$\lambda_{\text{eff}} \text{ (mm)}$	$Z_0 \text{ } (\Omega)$	$\lambda_{\text{eff}} \text{ (mm)}$
2.34 GHz	130.3	115.3	90.0	110.7
2.35 GHz	130.4	115.0	90.1	110.0
2.36 GHz	130.6	114.0	90.1	109.7
2.37 GHz	130.7	113.8	90.2	109.2
2.38 GHz	130.8	113.3	90.2	108.8
2.39 GHz	131.0	112.8	90.3	108.3
2.40 GHz	131.1	112.4	90.3	107.8

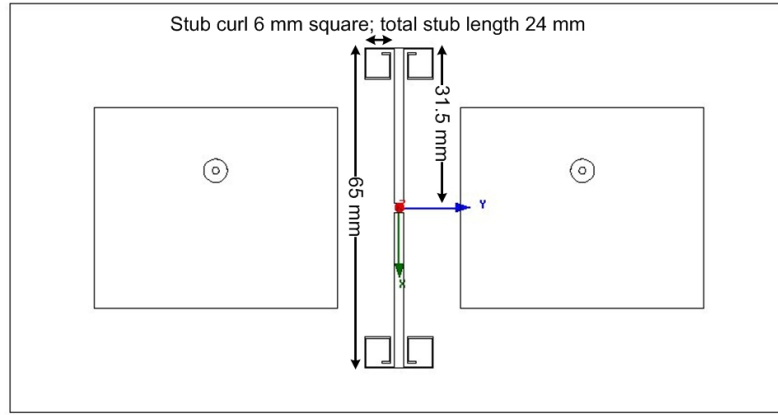


Figure 5.1: Mustache ground plane slot design on H-plane base system configuration.

will each be terminated with two stubs so that they resonate at 2.37 GHz. At this frequency the circuit model predicts that the stub lengths should be 23.3 mm, but best performance was obtained when the length was corrected to 24 mm. The stubs are spiraled to reduce the slot structure's footprint, which may be the reason a length correction was required. The resulting structure is shown in Figure 5.1.

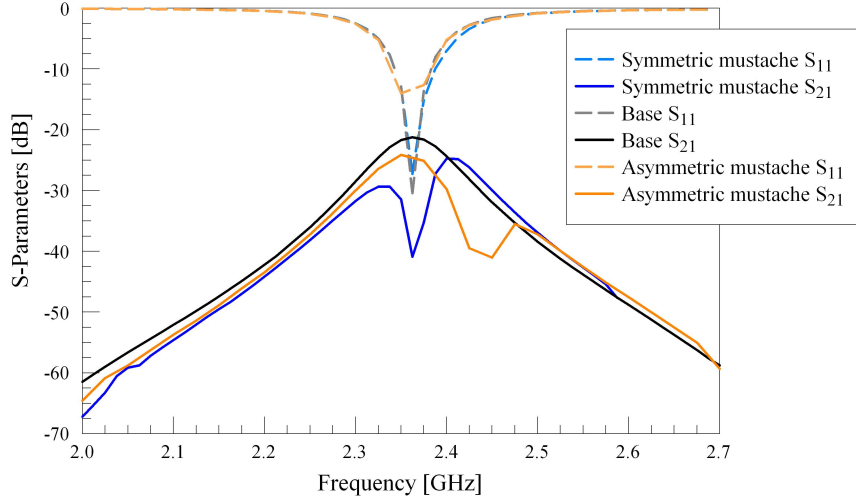


Figure 5.2: Simulated S_{21} for H-plane base configuration, symmetric mustache slot structure, and asymmetric mustache slot structure (simulated results from Ansoft HFSS).

5.2.1 Results

In order to introduce a dual resonance, an asymmetric mustache design was also attempted. The total structure length was still 65 mm, but the individual line lengths were changed to 31 mm and 32 mm, rather than being equal. Simulated insertion loss data for the H-plane base configuration, symmetric mustache design, and an asymmetric mustache design (l_1 is 31 mm in one mustache structure and 32 mm in the other) are shown in Figure 5.2. The presence of the symmetric mustache slots decreases S_{21} by 7 dB at the operating frequency. The frequency of the asymmetric mustache design's slot-induced dip moves up in frequency relative to the symmetric design, but no second slot-induced dip is introduced. Radiation patterns for the mustache designs with both antennas active are shown in Figures 5.3 through 5.6. The slot structure does not significantly change the radiation pattern of the antenna system.

Measured insertion loss data for the H-plane base configuration, symmetric mustache design, and asymmetric mustache design are shown in Figure 5.7. The

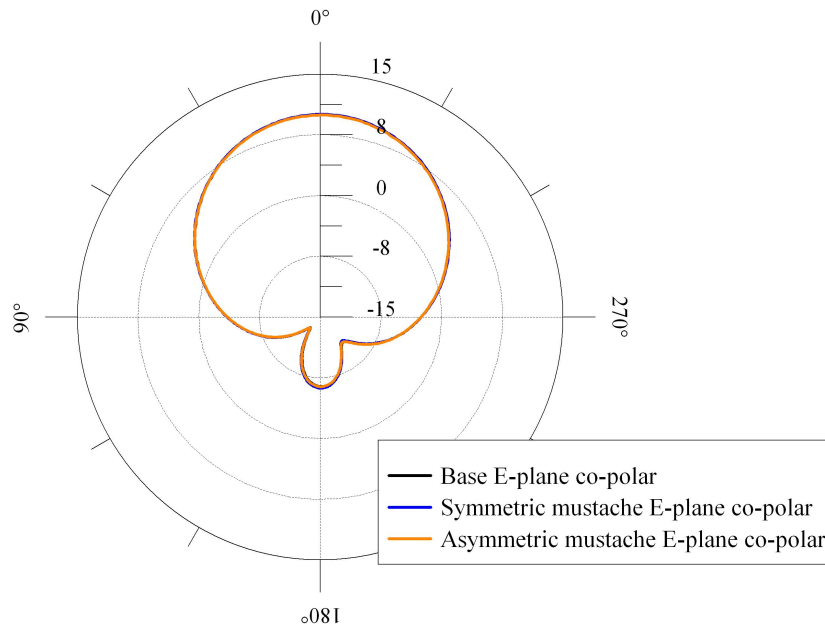


Figure 5.3: E-plane realized co-polar gain (in dB) of H-plane base configuration (black line) and systems with symmetric and asymmetric mustache slot structures (blue and orange lines, respectively), (simulated results from Ansoft HFSS).

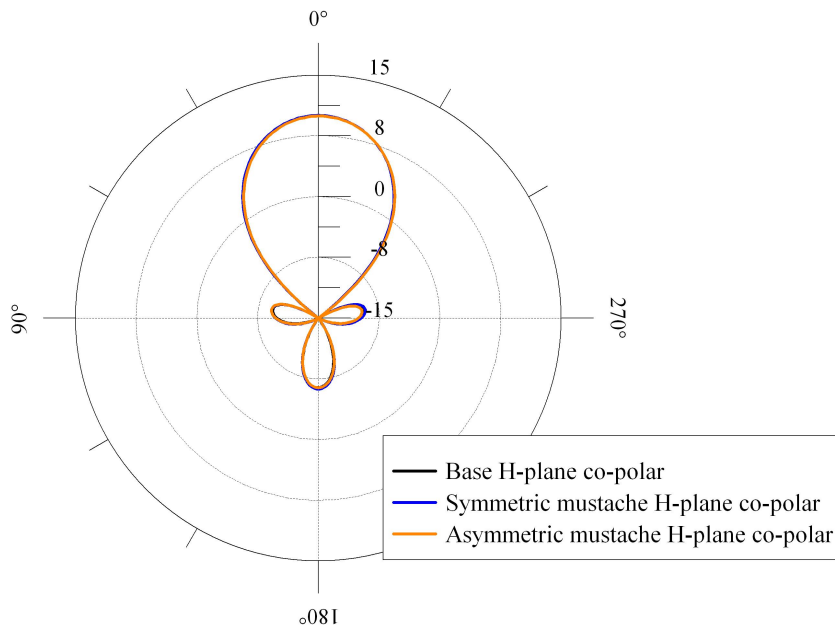


Figure 5.4: H-plane realized co-polar gain (in dB) of H-plane base configuration (black line) and systems with symmetric and asymmetric mustache slot structures (blue and orange lines, respectively), (simulated results from Ansoft HFSS).

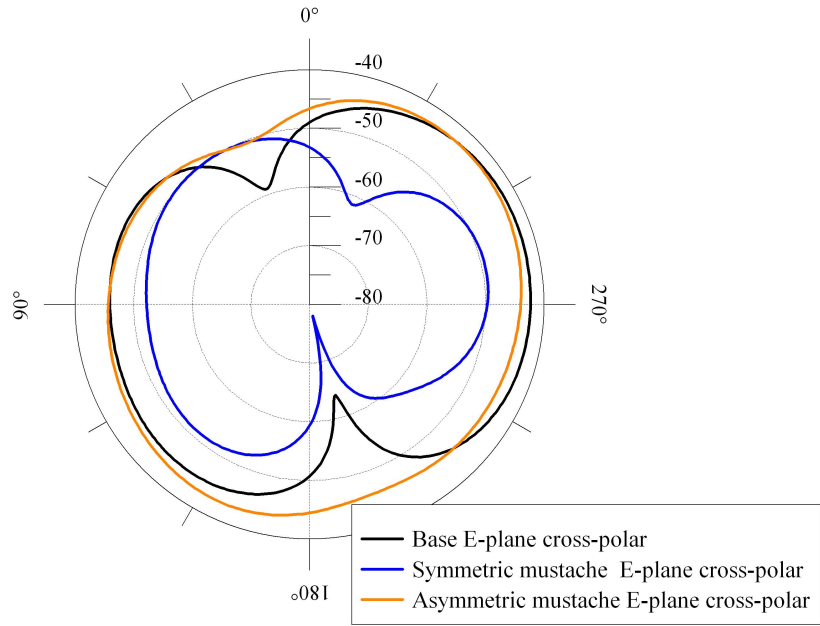


Figure 5.5: E-plane realized cross-polar gain (in dB) of H-plane base configuration (black line) and systems with symmetric and asymmetric mustache slot structures (blue and orange lines, respectively), (simulated results from Ansoft HFSS).

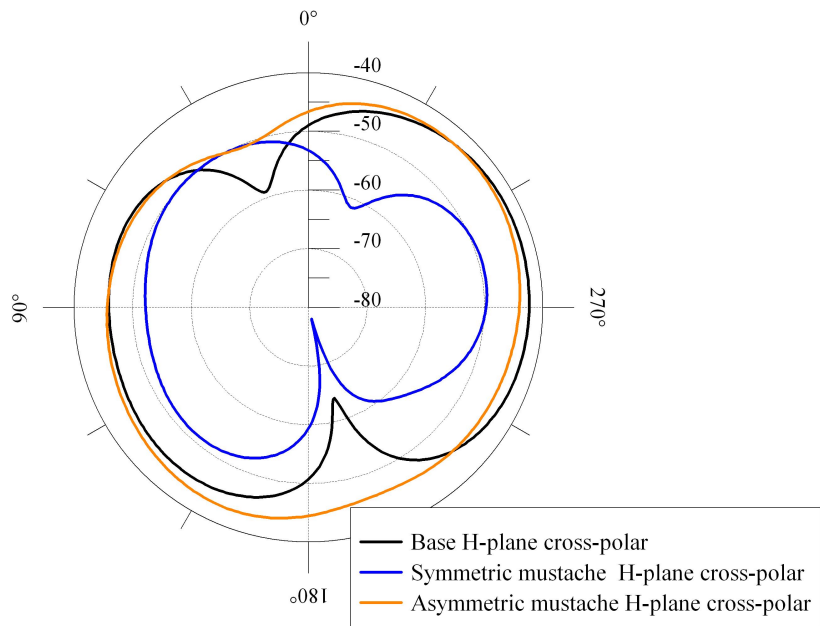


Figure 5.6: H-plane realized cross-polar gain (in dB) of H-plane base configuration (black line) and systems with symmetric and asymmetric mustache slot structures (blue and orange lines, respectively), (simulated results from Ansoft HFSS).

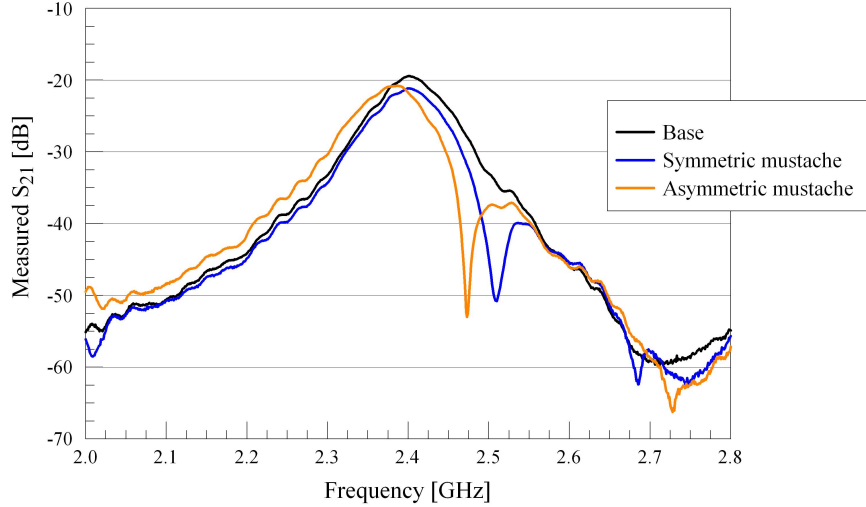


Figure 5.7: Measured S_{21} for H-plane base configuration, symmetric mustache slot design, and asymmetric mustache slot design.

asymmetric mustache design's S_{21} trace agrees with the simulated data, showing a single slot-induced dip near 2.5 GHz. The fabricated symmetric mustache design, compared to its model in simulation, undergoes a frequency shift relative to the antenna operating frequency. The most likely explanation for this is fabrication inaccuracy due to the very narrow width of the stub slots.

5.3 Conclusions

This chapter presented a technique for the design of slot resonators for inclusion in a ground plane to improve isolation between nearby antennas. Simulated results showed that the symmetric slot structure reduced S_{21} between the two antennas by 7 dB. In measured data, the slot-induced local minimum in the symmetric slot structure system's S_{21} was shifted in frequency relative to the operating frequency of the antenna and its position in simulated results.

CHAPTER 6

CONCLUSIONS

In this dissertation, we set out to improve the analysis and design techniques available for ground plane slot structures for isolation of cosited microstrip antennas. First, we examined the performance of reported designs. The scaling behavior of the existing designs implied that antenna orientation had some effect on the mode of slot excitation. By implementing the reported ground plane slot designs in systems with various substrate permittivities, center frequencies, and antenna orientations, we identified some excitation modes for ground plane slot structures and some characteristics of their excitation behavior. We developed a circuit model that accounts for mutual coupling between two patch antennas and an arbitrary ground plane slot structure, which requires a calculation of the self and mutual admittances of the ground plane slots and the equivalent radiating slots of the patch antennas. Since the antennas and slots are well within one another's near fields, this calculation must be carried out numerically. Through the circuit model we arrived at some simple design guidelines: the ground plane slot structure should have parallel-resonant behavior in order to have very small Y_{SS} ; and in order to isolate two antenna edge slots i and j their mutual admittances should satisfy this approximate condition:

$$Y_{ij} \pm Y_{iS}Y_{Sj}/Y_{SS} = 0 \tag{6.1}$$

In Equation (6.1), the sign of the second term is determined by the direction of voltage definition across the equivalent slots representing the antennas' radiating edges, which is a consequence of the antennas' orientation with respect to one another and the choice of i and j . These mutual admittances still must be either calculated or estimated, but a simple enough resonator design can be tuned to approximate the above condition. To that end, a novel ground plane slot resonator was introduced which has an explicit design process for determination of its resonant frequency. The design was simple enough that its admittance characteristics are transparently tunable by varying slot widths. Additionally, the structure did not introduce any limitations on ground plane geometry. These last two features are improvements over other reported designs.

Future work on this topic might investigate how mutual admittances and mode admittances are affected by slot and antenna geometries. Since the radiation and near-field components of a slot's or antenna's field have different phases and decay rates, phase is not linear with distance in closely packed situations. Although engineers can probably estimate the sign of X_{ij} for simple slot shapes, more rule-of-thumb information in this area could greatly simplify the design of ground plane slot isolation structures.

In general, the information provided here can be helpful in the development of more sophisticated structures for antenna isolation. The excitation and mode investigation revealed behavior that could be exploited for polarization-agile systems. Understanding of the circuit model and mutual admittance behavior is crucial for the development of multiband or wideband designs. Finally, since the circuit model represents merely a system of coupled resonators, there is no reason this technique should be limited to slots. A resonator printed on top of the substrate could also potentially provide isolation, and the designer would not face the threat of leaking radiation into the backplane. The EBG structure

in [3] is printed on top of the substrate, but a resonator designed along the guidelines presented here would not necessarily require the fabrication of such fine features.

REFERENCES

- [1] D. V. Campbell, P. W. Dubowicz, and R. T. Hoverter, Highly Decoupled Cosited Antennas, U.S. Patent 4 700 196, August, 1986.
- [2] D. Sievenpiper, L. Zhang, R. Broas, N. Alexopolous, and E. Yablonovitch, “High-impedance electromagnetic surfaces with a forbidden frequency band,” *IEEE Transactions on Microwave Theory and Techniques*, vol. 47, no. 11, pp. 2059–2074, Nov. 1999.
- [3] M. Abedin and M. Ali, “Effects of a smaller unit cell planar ebg structure on the mutual coupling of a printed dipole array,” *IEEE Antennas and Wireless Propagation Letters*, vol. 4, pp. 274–276, 2005.
- [4] C.-Y. Chiu, C.-H. Cheng, R. Murch, and C. Rowell, “Reduction of mutual coupling between closely-packed antenna elements,” *IEEE Transactions on Antennas and Propagation*, vol. 55, no. 6, pp. 1732–1738, June 2007.
- [5] G. Alvey, “Investigation of techniques for isolating cosite microstrip patch antennas,” M.S. thesis, University of Illinois at Urbana-Champaign, 2006.
- [6] C. Eswarappa, R. Anderson, and F. Kolak, “Periodic filters for performance enhancement of millimeter-wave microstrip antenna arrays,” *2004 IEEE MTT-S International Microwave Symposium Digest*, vol. 1, pp. 353–356, June 2004.
- [7] Ansoft HFSS version 11.1.3, 2008.
- [8] R. Jedlicka, M. Poe, and K. Carver, “Measured mutual coupling between microstrip antennas,” *IEEE Transactions on Antennas and Propagation*, vol. 29, no. 1, pp. 147–149, Jan. 1981.
- [9] P. Haddad and D. Pozar, “Anomalous mutual coupling between microstrip antennas,” *IEEE Transactions on Antennas and Propagation*, vol. 42, no. 11, pp. 1545–1549, Nov. 1994.
- [10] B. A. Munk, *Frequency Selective Surfaces*. New York, NY: John Wiley & Sons, 2000.

- [11] K. C. Kerby and J. T. Bernhard, "Analysis of ground plane structure for reduction of coupling between cosited microstrip antennas," in *Proceedings of the 2008 Antenna Applications Symposium*, Allerton Park, Monticello, IL, 2008, pp. 454–462.
- [12] R. Munson, "Conformal microstrip antennas and microstrip phased arrays," *IEEE Transactions on Antennas and Propagation*, vol. 22, no. 1, pp. 74–78, Jan. 1974.
- [13] E. H. van Lil and A. R. van de Capelle, "Transmission line model for mutual coupling between microstrip antennas," *IEEE Transactions on Antennas and Propagation*, vol. 32, no. 8, pp. 816–821, Aug. 1984.
- [14] B. Nauwelaers and A. van de Capelle, "Integrals for the mutual coupling between dipoles or between slots: With or without complex conjugate?" *IEEE Transactions on Antennas and Propagation*, vol. 36, no. 10, pp. 1375–1381, Oct. 1988.
- [15] C. A. Balanis, *Advanced Engineering Electromagnetics*. New York, NY: John Wiley & Sons, 1989.
- [16] R. F. Harrington, *Time-Harmonic Electromagnetic Fields*. New York, NY: John Wiley & Sons, 2001.
- [17] H. Pues and A. van de Capelle, "Accurate transmission-line model for the rectangular microstrip antenna," *IEE Proceedings H - Microwaves, Optics and Antennas*, vol. 131, no. 6, pp. 334–340, December 1984.
- [18] A. Bhattacharyya and R. Garg, "Effect of substrate on the efficiency of an arbitrarily shaped microstrip patch antenna," *IEEE Transactions on Antennas and Propagation*, vol. 34, no. 10, pp. 1181–1188, Oct 1986.
- [19] J. L. Volakis, *Antenna Engineering Handbook*. New York, NY: McGraw-Hill Co., 2007.
- [20] R. Janaswamy and D. Schaubert, "Characteristic impedance of a wide slotline on low-permittivity substrates (short paper)," *IEEE Transactions on Microwave Theory and Techniques*, vol. 34, no. 8, pp. 900–902, Aug. 1986.

AUTHOR'S BIOGRAPHY

Kiersten C. Kerby received the B.S. degree in electrical engineering in 2003 and the M.S. degree in electrical engineering in 2005, both from the University of Illinois at Urbana-Champaign. She received the IEEE Antennas and Propagation Scholarship in 2006, and was a Bell Labs Graduate Research Fellow in the 2006, 2007, and 2008 school years. Following completion of her Ph.D., Kerby will begin work for MITRE Corporation as an engineer in its electromagnetics group.